This is the peer-reviewed, final accepted version for American Mineralogist, published by the Mineralogical Society of America.
The published version is subject to change. Cite as Authors (Year) Title. American Mineralogist, in press.
DOI: https://doi.org/10.2138/am-2022-8057. http://www.minsocam.org/

Revision2

word count: 9041

Enhanced weathering in the seabed: rapid olivine dissolution and iron sulfide formation in submarine volcanic ash

Wolf-Achim Kahl[1,2,*], Andreas Klügel[1], Wolfgang Bach[1,3] & M. Mangir Murshed[2,4]

[1]Department of Geosciences, University of Bremen, Bremen, Germany

[2]MAPEX Center for Materials and Processes, University of Bremen, Bremen, Germany

[3]MARUM Center for Marine Environmental Sciences, University of Bremen, Bremen, Germany

[4]Institute of Inorganic Chemistry and Crystallography, University of Bremen, Bremen, Germany

*corresponding author, mailto: wakahl@uni-bremen.de

Abstract. In basaltic volcanic ash recovered from a seamount at 3000 m water depth we discovered marcasite and pyrite precipitation within cavities that formed by partial to complete dissolution of olivine. In places, these cavities are reminiscent of negative crystal shapes, elsewhere they apparently continue along cracks. In strong contrast, adjacent volcanic glass shows little, if any, evidence for dissolution. The FeS_2 precipitates were commonly found to be conjoined and planar aggregates, occurring in the center of the voids. Their maximum volume fraction in relation to the void space as determined by 2D and 3D imaging techniques corresponds to the amount of iron released by olivine dissolution. Almost all occurrences of FeS_2 precipitation are related to Cr-spinel

Always consult and cite the final, published document. See http:/www.minsocam.org or GeoscienceWorld

This is the peer-reviewed, final accepted version for American Mineralogist, published by the Mineralogical Society of America.
The published version is subject to change. Cite as Authors (Year) Title. American Mineralogist, in press.
DOI: https://doi.org/10.2138/am-2022-8057. http://www.minsocam.org/

inclusions in the former olivine. We propose that rapid olivine dissolution was initiated by reduced, H_2S-bearing fluids at olivine grain boundaries or surfaces exposed by cracks. Many of these cracks are connected to spinel grains, where the iron liberated from olivine is mineralized as FeS_2, initially facilitated by heterogeneous nucleation. Subsequent pyrite and/or marcasite precipitation occurred as overgrowth on existing FeS_2 aggregates. The particular chemical environment of low-pH, hydrogen sulfide-bearing fluids may have enhanced olivine dissolution by (i) keeping Fe in solution and (ii) sequestering important quantities of Fe as FeS_2. The in-situ oxidation of ferrous Fe and precipitation of ferric hydroxides at the olivine surface commonly observed in oxic environments was obviously impeded. It would have slowed down olivine dissolution to rates more similar to the dissolution of basaltic glass. We have no direct indication that the process of rapid olivine dissolution was aided by subseafloor life. However, the presence of fibrous structures with small sulfide particles could indicate a late colonization of sulfate-reducing bacteria that may add an additional path of iron fixation.

Keywords: Olivine, pyrite, marcasite, seamount, Canary Islands, dissolution, alteration, X-ray microscopy

INTRODUCTION

Iron sulfide formation pathways are commonly linked to the degradation of organic matter (see Roberts, 2015, and references therein). Examples include macroscopic iron sulfide nodules as remineralization of large-scale sedimentary organic matter fragments (Jiang et al., 2001), or formation of microscopic iron sulfide aggregates formed by remineralization of organic matter within microfossil chambers (Passier et al., 1997;

Always consult and cite the final, published document. See http:/www.minsocam.org or GeoscienceWorld

This is the peer-reviewed, final accepted version for American Mineralogist, published by the Mineralogical Society of America.
The published version is subject to change. Cite as Authors (Year) Title. American Mineralogist, in press.
DOI: https://doi.org/10.2138/am-2022-8057. http://www.minsocam.org/

Roberts et al., 2005). In sulfidic environments, iron-bearing detrital minerals undergo drastic alteration (see review of Roberts, 2015): hydrogen sulfide, which in many near-surface geochemical environments is a byproduct of bacterial sulfate reduction or anaerobic oxidation of methane, reacts with Fe^{2+} released from detrital minerals by dissolution to form iron sulfide minerals (mackinawite, greigite, and pyrite). It is not uncommon that marcasite (FeS_2, orthorhombic) or pyrite (FeS_2, cubic) replace greigite (Fe_3S_4, cubic) and mackinawite ($(Fe,Ni)_{1+x}S$ (x = 0-0.07), tetragonal) when an excess of H_2S is present (Hunger and Benning, 2007; Posfai et al., 1998; Roberts, 2015).

To our knowledge, the presence of sulfides connected with intense dissolution of olivine in a submarine volcanic setting has not been described so far. It is unclear, if this is a consequence of sparse sampling or of limited preservation of the appropriate boundary conditions for sulfide formation / conservation in this particular geological setting.

This communication seeks to unravel the formation of a striking reaction texture of FeS_2 within cavities in olivine phenocrysts, observed in glassy basaltic tephra from a seamount near the Canary Islands, Spain. While many of these cavities are reminiscent of negative shapes of their crystal host, elsewhere these voids appear to continue and broaden along cracks. Notably, the delicate FeS_2 precipitates hardly extend into the surrounding matrix of volcanic glass. We employ 2D and 3D spectroscopic methods to decipher mineral compositions and growth relations, and thermodynamic/kinetic computations to elucidate potential conditions and mechanisms of this reaction texture. Finally, we assess whether a microbial contribution to this process of olivine dissolution and iron sulfide formation is essential at all.

Always consult and cite the final, published document. See http:/www.minsocam.org or GeoscienceWorld

This is the peer-reviewed, final accepted version for American Mineralogist, published by the Mineralogical Society of America.
The published version is subject to change. Cite as Authors (Year) Title. American Mineralogist, in press.
DOI: https://doi.org/10.2138/am-2022-8057. http://www.minsocam.org/

69

70

71 ## GEOLOGICAL SETTING

72 The samples were recovered from Henry Seamount, a Cretaceous volcanic edifice 40
73 km southeast of El Hierro island, rising ~700 m above ~3700 m deep ocean floor (Fig.
74 1) (Gee et al., 2001; Klügel et al., 2011). The seamount was investigated and sampled
75 during R/V Meteor cruises M66/1 and M146, which provided evidence for Pleistocene to
76 present hydrothermal fluid circulation in the summit region. This evidence includes
77 locally dense coverage by shells from vesicomyid clams, occurrence of authigenic barite,
78 and localization of sites of weak fluid venting (Klügel et al., 2011; Klügel et al., 2020).
79 Most clams belong to the genus *Abyssogena southwardae*, which live in symbiosis with
80 sulfide-oxidizing bacteria and are mostly buried in H_2S-rich sediment at hydrothermal
81 vents and cold seeps (Krylova et al., 2010). Overall, the summit area of the seamount is
82 variably covered by pelagic sediment.

83 Some samples from the top of the seamount contain heterolithologic basaltic tephra
84 and dispersed basaltic rock fragments, suggesting rejuvenated volcanic activity (Klügel et
85 al., 2020). The tephra occurrences are commonly associated with clam shells, and basaltic
86 ash from one sample released H_2S during recovery on-board. The samples investigated
87 here represent the dominant lithology of an ash layer overlain by 10-13 cm of pelagic
88 sediment, recovered by gravity coring at 3145 m water depth; similar observations were
89 also made in ash samples from two other sites. A detailed description of this core (sample
90 22841-1) and the other samples is given in Klügel et al. (2018).

91

Always consult and cite the final, published document. See http:/www.minsocam.org or GeoscienceWorld

This is the peer-reviewed, final accepted version for American Mineralogist, published by the Mineralogical Society of America.
The published version is subject to change. Cite as Authors (Year) Title. American Mineralogist, in press.
DOI: https://doi.org/10.2138/am-2022-8057. http://www.minsocam.org/

92

93 ## METHODS

94 Detailed fabric inspections of single fragments were performed on a field emission
95 scanning electron microscope (SEM) Zeiss SUPRA 40 with a Bruker EDS-detector
96 XFlash 6|30 operated at 15 kV. Mineral analyses and fabric inspections of polished thin
97 sections of stray samples were performed on a Cameca SX-100 electron probe
98 microanalyzer (EPMA) at the Department of Geosciences, University of Bremen. Olivine
99 was analyzed with 15 kV / 30 nA, spinel with 15 kV / 15 nA, and sulfide with 20 kV / 20
100 nA, using a focused beam in all cases. Calibrations used natural minerals from the
101 Smithsonian Institution (Jarosewich et al., 1980), in-house standards, and pure elements
102 (Ni, Co); the built-in PAP correction was applied for data reduction. Analytical precision
103 and accuracy were controlled by regular analyses of Smithsonian reference standards
104 along with the samples (see Table 1 for average olivine, spinel and sulfide analyses, and
105 Table S1-3 in supplementary online material for individual analyses).

106 Stokes Raman spectra were collected at different locations of the polished section of
107 sample 22841. The spectra were recorded on a LabRam ARAMIS (Horiba Jobin Yvon)
108 Micro-Raman spectrometer equipped with a laser working at 633 nm and less than 20
109 mW output. The use of a 50x objective (Olympus) with a numerical aperture of 0.75
110 provides a focus spot of about 1 μm diameter when closing the confocal hole to 200 μm.
111 By usage of a neutral density filter (setting D1, 90% reduction) the laser power on the
112 sample surface was estimated to be about 0.33 mW. Raman spectra were collected in the
113 range between 100 cm^{-1} and 1000 cm^{-1} with a spectral resolution of approximately 2 cm^{-1}
114 using a grating of 1800 grooves/mm and a thermoelectrically cooled CCD detector

Always consult and cite the final, published document. See http:/www.minsocam.org or GeoscienceWorld

This is the peer-reviewed, final accepted version for American Mineralogist, published by the Mineralogical Society of America.
The published version is subject to change. Cite as Authors (Year) Title. American Mineralogist, in press.
DOI: https://doi.org/10.2138/am-2022-8057. http://www.minsocam.org/

(Synapse, 1024 x 256 pixels). The Rayleigh position and the linearity of the spectrometer were calibrated against the silicon signal and the emission lines of a neon lamp, respectively.

For 3D X-ray microscopy (XRM), two particles (olivine single grain: sample 22841-1A-SG; olivine multiple grains aggregate: 22841-1A-MGA) were glued by nail polish onto the tip of a graphite pencil mine. Both particles were scanned in 360° rotation scans conducted with the 3D X-ray microscope ZEISS Xradia 520 system of the MAPEX Center for Materials and Processes, University of Bremen, Germany. Particle 22841-1A-SG was scanned in overview mode with 1.30 µm per voxel and a beam energy of 90 kV and an energy flux of 89 µA (and ZEISS filter LE3), and a smaller volume of interest (VOI) of this sample was scanned with 0.36 µm per voxel (90 kV, 89 µA, filter LE3). Particle 22841-1A-MGA was scanned in overview mode with 2.44 µm per voxel (60 kV, 83 µA, filter LE3), and a smaller VOI was scanned with 0.78 µm per voxel (80 kV, 88 µA, filter LE3). Correction of ring artefacts and reconstruction of the spatial information on the linear attenuation coefficient in the samples was done using the ZEISS Reconstructor software. For each particle, an image volume of ca. 1000 x 1000 x 1000 voxels was available. All subsequent processing of volume data (e.g., rendering, filtering the raw data, segmentation, surface generation, 3D quantitative image analysis of iron sulfide volume fractions) was done using Avizo 2019 (FEI). For visualization of volume reconstructions and single slices, the Avizo filter module *RekursiveExponential* was used in 3D mode; for quantitative 3D image analyses of void and iron sulfide volume, prior to segmentation and binarization, this step was followed by a Non-*LocalMeans* filtering in 3D mode. Avizo module *AmbientOcclusion* was chosen to discriminate cavities inside

Always consult and cite the final, published document. See http:/www.minsocam.org or GeoscienceWorld

This is the peer-reviewed, final accepted version for American Mineralogist, published by the Mineralogical Society of America.
The published version is subject to change. Cite as Authors (Year) Title. American Mineralogist, in press.
DOI: https://doi.org/10.2138/am-2022-8057. http://www.minsocam.org/

138 volcanic ash particles from the surrounding region (Titschack et al., 2018). Avizo was
139 also used to determine the volume fractions of iron sulfide in 2D electron microprobe
140 BSE images.

141 In the reaction path modeling, volcanic glass, olivine, and organic carbon were reacted
142 with seawater at 5°C using Geochemist's Workbench 7.0 (Bethke, 1996). The system had
143 1 kg of seawater, 10 g of glass, 2 g of olivine, and 0.1 g of organic carbon. This high
144 water-to-rock ratio was chosen to reflect the porous nature of the tephra layer in the
145 shallow seabed. Graphite represents organic carbon, while fayalite represents olivine in
146 the model. The reaction rates were assumed to be slowest for glass (10^{-16} mol $cm^{-2}s^{-1}$),
147 fastest for organic carbon (5 10^{-13} mol $cm^{-2}s^{-1}$) and intermediate for olivine (10^{-15} mol $cm^{-2}s^{-1}$). These rates are reflecting experimental constraints on the reaction rates of olivine
149 and basaltic glass at neutral pH (Oelkers et al., 2018; Oelkers and Gislason, 2001). We
150 used rates lower than the ones measured at 25°C to account for the lower temperature
151 (5°C). Empirical observations of breakdown rates of moderately old (100-1000 yrs)
152 organic matter in seafloor sediments (Middelburg, 1989) was used to approximate
153 graphite dissolution rate in the model. Thermodynamic data of minerals and aqueous
154 species are from SUPCRT92 [Johnson et al. (1992) with updates from Wolery and Jove-
155 Colon (2004)]. The thermodynamic properties of the volcanic glass were computed using
156 a polyhedral approach for the average composition of sample 22841-1A (Klügel et al.,
157 2020). Gibbs energies, entropies, volumes, and Maier-Kelly coefficients of the
158 constituent oxides were taken from Helgeson et al. (1978) and updates in Wolery and
159 Jove-Colon (2004). Equilibrium constants for dissolution reactions of the model glass

Always consult and cite the final, published document. See http:/www.minsocam.org or GeoscienceWorld

This is the peer-reviewed, final accepted version for American Mineralogist, published by the Mineralogical Society of America.
The published version is subject to change. Cite as Authors (Year) Title. American Mineralogist, in press.
DOI: https://doi.org/10.2138/am-2022-8057. http://www.minsocam.org/

160 composition were computed using aqueous species data from SUPCRT92 (Johnson et al.,
161 1992) for a pressure of 25 MPa.

162

163

164 # RESULTS

165 ## Petrography and microfabric on the grain scale

166 The ash particles investigated here consist of fresh glass of alkali basaltic composition
167 with olivine phenocrysts (termed ash type 1 in Klügel et al., 2020). Olivine is euhedral to
168 subhedral, up to 2 mm in size, and occurs isolated or in clusters. The crystals show a
169 narrow compositional range of $Fo_{79.5\text{-}82.6}$ (average $Fo_{81.5}$), 0.23-0.39 wt% CaO, 0.18-0.31
170 wt% NiO, and no systematic zonation (Table 1). They contain inclusions of spinel with
171 Cr# = molar Cr/(Cr+Al) of 0.45–0.53, Mg# = molar Mg/(Mg+Fe^{2+}) of 0.39–0.50, and
172 Fe^{3+}/Fe^{tot} of 0.40-0.45 (Table 1); occasional spinel microphenocrysts in the glass, and
173 within iron sulfide precipitates, have similar compositions. By using the glass analyses in
174 Klügel et al. (2020) and the Fe^{2+}-Mg partition coefficient between olivine and melt after
175 Toplis (2005), we obtain a melt Fe^{3+}/Fe^{tot} ratio of 0.34.

176 Many olivine phenocrysts show pronounced development of iron sulfide within
177 cavities inside the crystals (Figs. 2b and c). In places, these cavities are reminiscent of
178 negative crystal shapes (Fig. 3a and b), elsewhere they apparently continue along cracks.
179 Similar sulfide formation, albeit far less common and less intense, is found along cracks
180 in some clinopyroxene phenocrysts in lithologically different ash fragments (Fig. 2a).
181 Where cavities meet both olivine and host glass, SEM investigations revealed very
182 limited dissolution features of the glass (Fig. 3b and c). In some cases, cavities clearly

Always consult and cite the final, published document. See http:/www.minsocam.org or GeoscienceWorld

This is the peer-reviewed, final accepted version for American Mineralogist, published by the Mineralogical Society of America.
The published version is subject to change. Cite as Authors (Year) Title. American Mineralogist, in press.
DOI: https://doi.org/10.2138/am-2022-8057. http://www.minsocam.org/

discernible as negative shapes of olivine crystals are entirely devoid of olivine material (Fig. 4a, c). Even in these cavities, iron sulfide precipitation does not appear to be irregular, but organized in relation to initial cracks or microfissures in the former olivine host.

Microprobe analyses of the sulfides (Table 1) indicate FeS_2 stoichiometry with some Fe replaced by Ni (0.35-0.87 wt%) and Mn (0.39-1.84 wt%). The serrate characteristic of many sulfide crystal shapes in SEM images (Fig. 3) clearly point to marcasite, forming conjoined, planar aggregates with a bead chain aspect in profile. Within olivine crystals affected only by incipient dissolution, FeS_2 aggregates can be observed in the center of narrow voids in relation to initial cracks or microfissures (Fig. 4b). Inside larger dissolution cavities in olivine, or where olivine was completely dissolved, FeS_2 precipitation is also organized as chains or planar aggregates, and does not occur deliberately anywhere on a free olivine or glass surface (Figs. 3-4, Fig. 5). In places, where aggregates of several olivine grains are surrounded by glass matrix (Fig. 4a and b), XRM reveals that cavities in these associated grains may be multiply connected and form a complex pore network (Fig. S1, supplementary online material).

The baseline-corrected and normalized Raman spectra of FeS_2 analyzed at selected locations of the polished thin section are displayed over the 200 to 600 cm^{-1} spectral range in Fig. 6. Following Vogt et al. (1983) and Lutz and Müller (1991), and considering the measured spectral resolution, the assignment of Raman bands to symmetry modes for pyrite (Py) and marcasite (Mrc) has been made as follows: 324 cm^{-1} (combined A_g^{Mrc}, B_{2g}^{Mrc}, and B_{3g}^{Mrc}), 343 cm^{-1} (E_g^{Py}), 350 cm^{-1} (T_g^{Py}), 378 (combined A_g^{Py} and T_g^{Py}), 388 cm^{-1} (A_g^{Mrc}), 398 cm^{-1} (B_{1g}^{Mrc}), 430 cm^{-1} (T_g^{Py}), 448 cm^{-1} (B_{1g}^{Mrc}). The integrated area

Always consult and cite the final, published document. See http:/www.minsocam.org or GeoscienceWorld

This is the peer-reviewed, final accepted version for American Mineralogist, published by the Mineralogical Society of America.
The published version is subject to change. Cite as Authors (Year) Title. American Mineralogist, in press.
DOI: https://doi.org/10.2138/am-2022-8057. http://www.minsocam.org/

206 under the bands at about 324 cm^{-1} and 343 cm^{-1}, respectively, was used to distinguish
207 between pyrite and marcasite. Moreover, considering that their differential Raman
208 scattering cross sections are similar, a quantitative approach has been performed.

209 The Raman spectra reveal the presence of both pyrite and marcasite in most of the
210 analyzed locations (Fig. 6, fit results are given in Table 2). Pure pyrite spectra were
211 observed in at least two locations (G1-11 and G1-14, Fig. 6b and c, respectively). A pure
212 marcasite phase was not identified within the investigated locations of the grains.
213 However, at G2-01 (Fig. 6d) shows that the location is comprised of about 97% marcasite
214 along with a minor (3%) pyrite phase fraction.

215

216 **Relation between cavity volume and iron sulfide content**

217 Cavities completely filled with iron sulfide were not observed in any olivine. By
218 means of 2D (derived from BSE images, Fig. 7a-e) and 3D (derived from reconstructed
219 XRM image volumes, Fig. 7f) quantitative digital image analysis, iron sulfide contents in
220 voids within olivine single crystals were found to range between 17.4 area% and 24.0
221 area%, and between 18.1 and 19.4 vol%. XRM analysis of the second sample
222 (supplementary Fig. S1), an aggregate consisting of several attached olivine grains
223 surrounded by a glass matrix, revealed an uneven distribution of iron sulfide
224 precipitation. The volume fraction of iron sulfide in the largest void, extending over six
225 olivine crystals, reached only 4.2 vol% (Fig. $7g_1$). In comparison, a high-resolution scan
226 of a region within the same aggregate reveals a degree of iron sulfide void filling of 10.1
227 vol% (Fig. $7g_2$). Altogether, the iron sulfide precipitation in the pore space of the olivine

Always consult and cite the final, published document. See http:/www.minsocam.org or GeoscienceWorld

This is the peer-reviewed, final accepted version for American Mineralogist, published by the Mineralogical Society of America.
The published version is subject to change. Cite as Authors (Year) Title. American Mineralogist, in press.
DOI: https://doi.org/10.2138/am-2022-8057. http://www.minsocam.org/

grain aggregate is substantially less than what was observed in voids within olivine single crystals hosted in other particles (see Table 3).

Fabric relation of iron sulfide and spinel

Whereas olivine is largely affected by dissolution processes, the host glass shows only minor etch pits and spinel exhibits no indication of dissolution. Spinel occurring within the volcanic glass or in olivine material unaffected by dissolution mostly exhibits euhedral to subhedral morphology (Fig. 8a). Likewise, spinel situated within cavities displays the very same morphology, and is mostly overgrown by the iron sulfide precipitates (Fig. 4a, Fig. 5b, Fig. 8, and supplementary Fig. S3). Moreover, detailed observations of some sites visible in Figs. 4a, 8b, and S3 indicate that iron sulfide growth was not initiated as alteration of spinel rims to sulfide, but by overgrowth on the existing spinel surface.

Further potential nucleation sites of small sulfide particles

High-resolution 3D X-ray microscopy imaging (Fig. 8b) shows that small sulfide particles (1-2 μm) are also observed along and/or within filamentous stalks connecting cavity-centered, aligned sulfide aggregates of up to 20-60 μm diameter, analogous to the strand of a bead chain. The XRM image material (0.36 μm voxel size, compare scale information in Fig. 8b) depicts these stalks to be less X-ray attenuating than the volcanic glass, and more similar to void space. As the particles investigated by 3D X-ray microscopy were neither cut nor ground and hence did not suffer any stress during

Always consult and cite the final, published document. See http:/www.minsocam.org or GeoscienceWorld

This is the peer-reviewed, final accepted version for American Mineralogist, published by the Mineralogical Society of America.
The published version is subject to change. Cite as Authors (Year) Title. American Mineralogist, in press.
DOI: https://doi.org/10.2138/am-2022-8057. http://www.minsocam.org/

sample preparation, the filamentous stalks could be preserved within the well-protected pore space inside the gravity core material in a desiccated manner. It is possible that these structures represent organic material; however, further investigations by e.g. Raman spectrometry cannot be carried out due to the inaccessibility of the interior of this particular ash particle.

DISCUSSION

Chemical environment for olivine dissolution and iron sulfide formation

Abundant FeS_2 precipitation within cavities created by olivine dissolution indicates the availability of reactive iron (likely derived from olivine dissolution) and sulfide in solution. Indeed, evidence of hydrogen sulfide at the sample sites is twofold: (i) the perception of hydrogen sulfide smell during sample recovery; and (ii) the spatial association of the samples to shells of vesicomyid clams on the top sediment layer. All known species of the genus *Abyssogena* have been observed in sulfide-rich habitats at hydrothermal vents and cold seeps (Krylova et al., 2010). Typically, *Abyssogena* live half-buried in the sediments, where the anterior part of the clam with the extendable foot has access to hydrogen sulfide.

Notably, the microfabric of FeS_2 precipitation within cavities resembling negative olivine crystal shapes indicates conditions of enhanced olivine dissolution. In contrast, volcanic glass adjacent to the olivine crystals was nearly unaffected by dissolution processes. Generally, basalt glass is observed to dissolve slightly more slowly (ca. 10^{-12} mol cm^{-2} s^{-1} at pH 3, and ca. 10^{-15} mol cm^{-2} s^{-1} at pH 6) (Flaathen et al., 2010; Gislason

Always consult and cite the final, published document. See http:/www.minsocam.org or GeoscienceWorld

This is the peer-reviewed, final accepted version for American Mineralogist, published by the Mineralogical Society of America.
The published version is subject to change. Cite as Authors (Year) Title. American Mineralogist, in press.
DOI: https://doi.org/10.2138/am-2022-8057. http://www.minsocam.org/

and Oelkers, 2003; Oelkers and Gislason, 2001) than olivine (ca. 10^{-12} mol cm^{-2} s^{-1} at pH 3, and ca. 10^{-14} mol cm^{-2} s^{-1} at pH 6) (Oelkers et al., 2018; Rimstidt et al., 2012) at 25°C and under oxic conditions. In contrast, the chemical environment of reducing, low-pH, sulfide-bearing fluids may enhance olivine dissolution by keeping Fe in solution and sequestering important quantities of Fe as FeS_2. Under these conditions in-situ oxidation of ferrous Fe and precipitation of ferric hydroxides at the olivine surface are impeded. These two processes may lower olivine reactivity and cause inhibition of olivine dissolution under oxic conditions (Gerrits et al., 2020). Similarly, experimental simulations by Wiggering et al. (1992) showed that subaqueous weathering under a CO_2-rich, H_2S-bearing, hypothetical Archean atmosphere was much more intense than under today's conditions: in this acidic environment, ferrous iron released by dissolution remained in solution. The effect of the addition of H_2S to fluids on silicate dissolution has been explored by Stefánsson et al. (2011) to simulate sequestration of H_2S into wastewater to be reinjected into the geothermal system Hellisheidi, Iceland. Their reaction path modelling showed that the accompanying decrease in pH resulted in undersaturation of Al-bearing silicates, but supersaturation with respect to sulfides.

As elements other than Fe were removed during olivine dissolution, the question arises whether the Fe in the precipitated FeS_2 was inherited entirely from the dissolved olivine material. A simple mass balance shows that complete fixation of Fe should result in ca. 20 vol% FeS_2 filling of the cavity created by olivine dissolution ($Fo_{81.5}$). Analyses of BSE images revealed iron sulfide fillings between 17.4 and 24.0 percent by area (Fig. 7a-e, and Table 3), and analyses of two cavities inside an olivine single crystal using reconstructed XRM scans yielded 18.1 and 19.4 volume percent, respectively. These

Always consult and cite the final, published document. See http:/www.minsocam.org or GeoscienceWorld

This is the peer-reviewed, final accepted version for American Mineralogist, published by the Mineralogical Society of America.
The published version is subject to change. Cite as Authors (Year) Title. American Mineralogist, in press.
DOI: https://doi.org/10.2138/am-2022-8057. http://www.minsocam.org/

296 results suggest that dissolution of olivine has provided all iron necessary for iron sulfide
297 formation nearly in-situ inside olivine cavities (Fig. 7f). Notwithstanding, a highly-
298 connected cavity spanning over several grouped olivine crystals exhibits far less than
299 maximum iron sulfide fixation: Figure 7g depicts low 4.2 vol% iron sulfide precipitation
300 within the entire pore network, increasing to 10.1 vol% within a restricted region.
301 Apparently, not all Fe deliberated from dissolved olivine was fixated by iron sulfide
302 precipitation.

303 Although the serrate crystal shapes of the iron sulfides point to marcasite precipitation
304 from solution, the coincident presence of pyrite in most places (Fig. 6) indicates a more
305 complex FeS_2 fixation history. Locally, pyrite makes up a very high phase fraction in the
306 Raman spectra of the analyzed spots. While we could not find a systematic relation
307 between marcasite/pyrite ratios and petrographic features such as void size or crack
308 width, our data suggest that domains with high proportions of pyrite are co-located with
309 spinel (e. g., G-13 and G-14, Fig. 6c). In some locations concomitant red/blue-shift of the
310 frequencies has been observed for both phases irrespective of their proportion. For
311 instance, whereas the fitted frequencies at G1-11 correspond to those observed by Vogt et
312 al. (1983), a general blue shift has been identified at G1-14 (see supplementary Fig. S2).
313 The corresponding higher frequencies with broader line shape at G1-14 in general can be
314 explained by slightly different unit cell dimensions and, rather likely when considering
315 the geochemical environment of our investigated samples, by a spread in the distribution
316 of degree of crystallinity and average crystallite size. Of note, Bryant et al. (2017)
317 suggested that red shift of band positions can be associated with laser-induced heating
318 during Raman investigations, and that variations in the ratios of band intensities can arise

Always consult and cite the final, published document. See http:/www.minsocam.org or GeoscienceWorld

This is the peer-reviewed, final accepted version for American Mineralogist, published by the Mineralogical Society of America.
The published version is subject to change. Cite as Authors (Year) Title. American Mineralogist, in press.
DOI: https://doi.org/10.2138/am-2022-8057. http://www.minsocam.org/

due to differing crystallographic orientations of the Raman locations with respect to the laser's dominant polarization plane.

Can the observation of co-existing pyrite and marcasite be related to phase transformations induced by Raman laser heating? Xi et al. (2019) discussed such thermal transformation, and found that the minimum laser power for these reactions to occur is 2.87 mW (see their Fig. 6 and related text). In contrast, our Raman investigations were carried out with a substantially reduced the laser power on the sample surface of about 0.33 mW (by usage of a neutral density filter, see methods section). Moreover, during the measurements, we could not observe any change of either intensity of a given band or appearance/disappearance of any band. For these reasons we can exclude transformation induced by laser heating during our Raman analyses. However, variable proportions of Mrc and Py in the sulfide aggregates of the present study could be related to marcasite to pyrite transformation at hydrothermal conditions. In a recent study of an interface-coupled dissolution-reprecipitation reaction involving pyrrhotite, Yao et al. (2021) observed that Mrc to Py transformation in small particles (< 100 nm) can occur within a few months at 210 °C, a pH of 1, and a high sulfide saturation index. Although we do not know how these conditions relate to those of our study, the experiments of Yao et al. (2021) suggest that post-crystallization transformation of marcasite to pyrite may have contributed to the variable Mrc and Py proportions observed by us.

Commonly, marcasite is associated with iron sulfide formation at lower pH than estimated for pyrite formation (recently summarized in (Yao et al., 2021; Yao et al., 2020)). Precipitation of marcasite from hydrothermal solutions has been observed in experimental studies at pH values of 5 or lower (Murowchick and Barnes, 1986;

Always consult and cite the final, published document. See http:/www.minsocam.org or GeoscienceWorld

This is the peer-reviewed, final accepted version for American Mineralogist, published by the Mineralogical Society of America.
The published version is subject to change. Cite as Authors (Year) Title. American Mineralogist, in press.
DOI: https://doi.org/10.2138/am-2022-8057. http://www.minsocam.org/

342 Schoonen and Barnes, 1991). However, in more complex experimental environments or
343 natural systems, inhomogeneities can catalyze heterogeneous nucleation: Qian et al.
344 (2011) suggested that a coupled dissolution-reprecipitation reaction can have marcasite
345 replace pyrrhotite at low sulfide activity of the fluid and does not require low pH. These
346 authors also found that marcasite formed only on pyrrhotite grains, not on other parts of
347 their experimental autoclaves, which suggests an epitaxial nucleation at an incipient
348 reaction stage. Significant in respect to the iron sulfide microfabric relations observed in
349 this study, experiments of Schoonen and Barnes (1991) indicate that, in acidic solutions
350 below 100 °C, nucleation of FeS_2 is actually inhibited, although growth of existing
351 marcasite and pyrite is possible under these conditions.

352 The microfabric of conjoined, variably intergrown crystals (Barbee et al., 2020;
353 Welsch et al., 2012) constituting the iron sulfide aggregates of our study suggests an
354 increased reaction affinity (ΔG_r), at least during early growth of the center layer (Figs. 3,
355 7, and 8). This is in conspicuous contrast to the absence of nucleation sites of FeS_2 on
356 volcanic glass. Thus, the presence and intergrowth of two different iron sulfide
357 modifications does not necessarily reflect changes of boundary conditions such as
358 temperature or pH value. It is also unlikely to reflect transformation of the one
359 modification into the other, as we have discussed above. It could however indicate a
360 formation pathway that successfully overcame hindered nucleation. Pyrite may have
361 grown in the first place, and subsequent fixation of FeS_2 may have occurred as marcasite
362 precipitation**,** producing the serrate shapes observed. Potential indications of this growth
363 sequence are (i) the higher pyrite fraction in mixed iron sulfide analyses near spinel
364 (which is located prevalently in the center of the precipitates), and (ii) the serrate,

Always consult and cite the final, published document. See http:/www.minsocam.org or GeoscienceWorld

This is the peer-reviewed, final accepted version for American Mineralogist, published by the Mineralogical Society of America.
The published version is subject to change. Cite as Authors (Year) Title. American Mineralogist, in press.
DOI: https://doi.org/10.2138/am-2022-8057. http://www.minsocam.org/

365 marcasite-like shape of the outer parts of the iron sulfide precipitates (presumably fixated
366 later than the interior parts).

367

368 **Control on the sites of iron sulfide precipitation**

369 Our observation that FeS_2 precipitation is completely lacking at the surfaces of
370 volcanic glass and dissolving olivine evidently corroborates the finding of Schoonen and
371 Barnes (1991) that the rate of homogeneous FeS_2 nucleation is negligible in acidic
372 solutions. Instead, we observe that iron sulfide precipitation at an incipient stage is
373 inevitably linked to the presence of spinel inclusions in olivine (Figs. 4a, and 8, and S3).
374 In particular, Fig. $8b_4$ exemplarily depicts a stage of incipient growth of iron sulfide on
375 spinel. Regarding the inventory of available sites for heterogeneous FeS_2 nucleation,
376 spinel surfaces apparently provide the preferred opportunity for heterogeneous
377 nucleation, since olivine is dissolving, and volcanic glass is obviously not favoring iron
378 sulfide precipitation. The latter observation is particularly important, as it demonstrates
379 the requirement of a pre-existing crystal structure for heterogeneous nucleation of iron
380 sulfide to occur.

381 The idea of heterogeneous nucleation of marcasite is corroborated by the experimental
382 results of Qian et al. (2011) who reported epitaxial marcasite nucleation exclusively on
383 pyrrhotite grains and not on other parts of their autoclaves. Furthermore, we show that
384 FeS_2 precipitation has occurred dominantly where a spinel surface is connected to a
385 cavity within dissolved olivine. After heterogeneous nucleation on spinel grains has
386 occurred, iron sulfide can grow under conditions at which rates of homogeneous
387 nucleation are still low. If spinel surfaces are critical to the nucleation of iron sulfide, then

Always consult and cite the final, published document. See http:/www.minsocam.org or GeoscienceWorld

This is the peer-reviewed, final accepted version for American Mineralogist, published by the Mineralogical Society of America.
The published version is subject to change. Cite as Authors (Year) Title. American Mineralogist, in press.
DOI: https://doi.org/10.2138/am-2022-8057. http://www.minsocam.org/

388 a relationship between the abundance of both phases may be expected. Indeed, we found
389 that regions with minor spinel exposed at olivine dissolution surfaces within the
390 interconnected pore space of the olivine aggregates show less FeS_2 precipitation (see Fig.
391 S1).

392 These interpretations are in accordance with the results of 3D X-ray microscopy (Figs.
393 8 and S3), which unveiled nucleation sites on spinel, development of cavities around
394 spinel grains near the olivine dissolution surface, and the organization of FeS_2 aggregates
395 with spinel crystals enclosed therein. Raman spectroscopy showed that FeS_2 occurrences
396 close to spinel grains are dominated by pyrite. This supports our earlier notion that iron
397 sulfide formation initially proceeds via heterogeneous growth of pyrite on spinel (both of
398 cubic symmetry), joined by marcasite precipitation in later stages. Heterogeneous FeS_2
399 nucleation may occur directly on the spinel surface. It is conceivable that an alternative
400 iron sulfide formation pathway occurs via thin layers of greigite (Fe_3S_4; the thio-spinel of
401 iron), a phase not uncommon to submarine iron sulfide formation in a sedimentary setting
402 (Rickard, 2012; Roberts, 2015). In this case, greigite rather than FeS_2 may have been the
403 phase to grow initially on the spinel surface, providing opportunity for subsequent
404 nucleation of pyrite. However, we did not detect any greigite by our EPMA or Raman
405 investigations at the resolution used. At this point, we cannot resolve by which
406 mechanisms heterogeneous nucleation actually occurred, and whether epitaxial growth
407 played a major role.

408

409 **Thermodynamic/kinetic constraints concerning formation pathway and timing**

Always consult and cite the final, published document. See http:/www.minsocam.org or GeoscienceWorld

This is the peer-reviewed, final accepted version for American Mineralogist, published by the Mineralogical Society of America.
The published version is subject to change. Cite as Authors (Year) Title. American Mineralogist, in press.
DOI: https://doi.org/10.2138/am-2022-8057. http://www.minsocam.org/

We conducted reaction path model calculations to determine if the formation of pyrite or marcasite is plausible in a system in which seawater interacts with basaltic glass, olivine, and organic carbon. The results in Fig. 10 show that pyrite is indeed expected to be the dominant secondary mineral in the early stages of evolution. Celadonite and smectite clay are predicted to form later in the sequence as the pool of solutes is more strongly affected by elements released by (slow) glass dissolution. When the organic carbon is oxidized and the reducing power for sulfate reduction is exhausted in the model, pyrite formation slows and eventually gives way to the formation of goethite and clay. In the mature stages of alteration, clay, oxide, and carbonate dominate the predicted assemblage of secondary minerals. This is consistent with what is observed in altered basalts from the ocean crust (e.g., Alt, 1995). Of particular importance in the modeling results is the episode between 100 and 10,000 years, during which pyrite is predicted to dominate the secondary mineral assemblage (Fig. 10). The assumption of reaction rates decreasing in the order of organic carbon, olivine, and glass is critical for the model to predict the abundant pyrite formation in the first couple of thousands of years. The model predicts organic carbon to become oxidized by sulfate, which is turned to sulfide. Iron is released from olivine dissolution, which is faster than the dissolution of glass by roughly an order of magnitude (Oelkers et al., 2018; Oelkers and Gislason, 2001). Iron then reacts with sulfide from bacterial sulfate reduction to form pyrite (or marcasite). Distinguishing between the two FeS_2 polymorphs in the model does not make any difference. Marcasite is predicted to form when pyrite formation is suppressed in the model, and its abundance curve is undistinguishable from that of pyrite in Fig. 10.

Always consult and cite the final, published document. See http:/www.minsocam.org or GeoscienceWorld

This is the peer-reviewed, final accepted version for American Mineralogist, published by the Mineralogical Society of America.
The published version is subject to change. Cite as Authors (Year) Title. American Mineralogist, in press.
DOI: https://doi.org/10.2138/am-2022-8057. http://www.minsocam.org/

The absolute reaction rates are poorly constrained, but our assumed factors of 10 and 500 by which the dissolution of olivine and reaction of organic carbon, respectively, is faster than glass dissolution are reasonable. Organic carbon reaction kinetics in the diagenetic system is controlled by microbial metabolism, as the reduced carbon is the electron donor in the catabolic reaction that uses sulfate as terminal electron acceptor. By as of yet unidentified mechanisms, the metabolic products of microbial sulfate reduction may enhance the difference in dissolution rates between olivine and volcanic glass. The more accelerated olivine dissolution is relative to the rate of basalt glass dissolution, the more pronounced is the dominance of pyrite in the secondary mineral assemblage in the incipient alteration stage, before clay-oxide-carbonate alteration eventually takes over. The mechanisms behind this enhanced weathering of olivine in the sulfate-reduction zone need to be examined and may involve microbially produced chelators that help solubilize the iron.

The predicted period for dominant pyrite formation between 100 and 10,000 years is consistent with a presumably young age of the fresh volcanic ash samples here studied. Precise age dates are lacking, but the spatial association between ash and clam shell fields led Klügel et al. (2020) to hypothesize that hydrothermal circulation and consequent colonization by vesicomyid *Abyssogena* clams were initiated by one or more pulses of volcanic activity. The age of the ash may thus be close to the radiocarbon ages of clam shells, which are in the range of a few ka to <20 ka (Klügel et al., 2011; Klügel et al., 2020). This age range would be consistent with a sediment coverage of the ash by <13 cm in the gravity core (Fig. 1b), and <20 cm in nearby grab samples, if a sedimentation rate of <7 cm/ka (Gee et al., 2001) is assumed.

Always consult and cite the final, published document. See http:/www.minsocam.org or GeoscienceWorld

This is the peer-reviewed, final accepted version for American Mineralogist, published by the Mineralogical Society of America.
The published version is subject to change. Cite as Authors (Year) Title. American Mineralogist, in press.
DOI: https://doi.org/10.2138/am-2022-8057. http://www.minsocam.org/

455

456 **Conceptual model for iron sulfide formation**

457 A most striking feature of the observed dissolution-precipitation reaction is that the
458 iron sulfide fillings are organized in a bead chain aspect and are centered in the cavities
459 (Figs. 7 and 8). Here we present a conceptual model for iron sulfide formation from
460 rapidly dissolving olivine (Fig. 9).

461 The key features are intracrystalline cracks within the olivine crystals, along which
462 low-pH, H_2S-bearing fluids could percolate (Fig. 9b). These cracks appear to develop
463 preferentially around spinel (see Welsch et al., 2012, their figure 11), likely during the
464 submarine eruption event or during magma ascent and decompression as a result of
465 different elastic properties and thermal expansion of spinel and host olivine. Facilitated
466 by high solubility of Fe^{2+} in the reduced fluids, rapid olivine dissolution proceeds at grain
467 boundaries and at surfaces exposed by the cracks. By heterogeneous nucleation of FeS_2
468 on spinel grains, pyrite and possibly marcasite precipitation can begin within very thin
469 fissures at an early stage of dissolution once Fe^{2+} is available (Fig. 9c-d). Continued
470 olivine dissolution enlarges these cracks forming cavities, and continued nucleation and
471 growth of pyrite and/or marcasite form aggregates centered within the growing gaps. A
472 cartoon representation of the chemical environment for rapid olivine dissolution and iron
473 sulfide formation is presented in Fig. 9a.

474

475 **Possible role of microbial interactions for olivine dissolution and/or FeS_2**
476 **precipitation**

Always consult and cite the final, published document. See http:/www.minsocam.org or GeoscienceWorld

This is the peer-reviewed, final accepted version for American Mineralogist, published by the Mineralogical Society of America.
The published version is subject to change. Cite as Authors (Year) Title. American Mineralogist, in press.
DOI: https://doi.org/10.2138/am-2022-8057. http://www.minsocam.org/

Although there are many studies that report microbial or fungial mediation of mineral dissolution reactions (Gerrits et al., 2020; Thiel et al., 2019; Welch and Banfield, 2002), the process of rapid olivine dissolution was not necessarily directly mediated by subseafloor life. The observation of smooth dissolution surfaces with negative crystal shapes point to a crystallographic-mineralogical control rather than microbe-aided olivine dissolution. Whereas microbial reduction of sulfate to sulfide may have produced the reducing environment required for the dissolution, an abiotic sulfide source from depth is also possible (Klügel et al., 2020).

The precipitation of iron sulfide aggregates investigated in this study may well be understood by epitaxial nucleation related to spinel and continued iron sulfide precipitation from low-pH and H_2S-bearing fluids (Fig. 9). When microbes exert crystallochemical control over the nucleation and growth of the mineral particles, distinctly different particle morphologies and narrow size distributions can develop (Bazylinski and Frankel, 2003). For instance, magnetotactic bacteria intracellularly produce greigite particles in the size range of 100 nm (Heywood et al., 1991; Posfai et al., 1998) that are aligned in μm-sized multiple chains, and extracellular biomineralization of greigite was reported by Gorlas et al. (2018). Furthermore, biomineralization producing extracellular, filamentous structures (Chan et al., 2011; Emerson et al., 2007; Hallbeck and Pedersen, 1991; Vigliaturo et al., 2020) has been linked to Fe(III)-rich filaments observed in the geological record (Alt, 1988; Hofmann et al., 2008; Little et al., 2004; Slack et al., 2007). Therefore, in the rock studied here, late colonization of sulfate-reducing bacteria may eventually have added a further path of iron fixation (Figs. 8b and

Always consult and cite the final, published document. See http:/www.minsocam.org or GeoscienceWorld

This is the peer-reviewed, final accepted version for American Mineralogist, published by the Mineralogical Society of America.
The published version is subject to change. Cite as Authors (Year) Title. American Mineralogist, in press.
DOI: https://doi.org/10.2138/am-2022-8057. http://www.minsocam.org/

499 9e): fibrous structures with small sulfide particles in extracellular stalks could well
500 contribute as nuclei for later iron sulfide growth sites.

501

502

503 **IMPLICATIONS**

504 Under sulfidic conditions, dissolution of olivine at the seafloor can be rapid and
505 greatly exceed glass dissolution rates. These conditions can be due to microbial
506 respiration of seawater sulfate to sulfide in marine sediments, or to influx of
507 hydrothermally sourced (abiotic) sulfide. The sulfide-bearing fluids enhance olivine
508 dissolution by preventing the formation of hydrous ferric oxide layers and sequestering
509 iron as FeS_2.

510 An important prerequisite of the effective fixation of Fe as iron sulfide may be the
511 opportunity of heterogeneous nucleation. There is no evidence for homogenous
512 nucleation of FeS_2. Instead, initial pyrite precipitation was facilitated by heterogeneous
513 nucleation on spinel grains exposed to the void space. Subsequent removal of Fe from
514 solution occurred exclusively by pyrite and marcasite precipitation as overgrowth on
515 existing iron sulfide aggregates.

516 The delicate structures of FeS_2 within voids created by olivine dissolution have not
517 been described before. They may represent a transient feature in seafloor alteration, as
518 progressive dissolution of volcanic glass causes the formation of Fe-oxyhydroxides and
519 clay minerals (iddingsitization), which is the commonly observed alteration feature in
520 seafloor basalts. The filling of former olivine voids by these later alteration phases and/or

Always consult and cite the final, published document. See http:/www.minsocam.org or GeoscienceWorld

This is the peer-reviewed, final accepted version for American Mineralogist, published by the Mineralogical Society of America.
The published version is subject to change. Cite as Authors (Year) Title. American Mineralogist, in press.
DOI: https://doi.org/10.2138/am-2022-8057. http://www.minsocam.org/

carbonates may obscure the earlier formed iron sulfides, making them a comparatively rare observation.

ACKNOWLEDGMENTS

W.A.K. and W.B. are grateful for funding by DFG Reinhart Koselleck Project [grant no. BA 1605/10-1], and AK acknowledges funding of the Henry Seamount research by DFG (grant KL1313/18-1). We gratefully acknowledge the reviews of Benjamin Malvoisin and an unknown reviewer.

Always consult and cite the final, published document. See http:/www.minsocam.org or GeoscienceWorld

This is the peer-reviewed, final accepted version for American Mineralogist, published by the Mineralogical Society of America.
The published version is subject to change. Cite as Authors (Year) Title. American Mineralogist, in press.
DOI: https://doi.org/10.2138/am-2022-8057. http://www.minsocam.org/

Figure Captions

Figure 1. (a) Location map of El Hierro island and Henry Seamount, made with GeoMapApp (Ryan et al., 2009); inset shows the Canary Islands. (b) Gravity core sample GeoB22841-1 taken from the summit of the seamount. It contains coarse basaltic ash investigated here, overlain by marine sediment.

Figure 2. Volcanic ash particles embedded in thin section (plane polarized light). (a) Survey of the different lithologies occurring in the volcanic ash layer. Several particles contain olivine or pyroxene crystals that exhibit sulfide-filled cavities. (b) Sulfide-filled cavity in volcanic glass where the former olivine has completely vanished. (c) Particle with olivines displaying tubular cavities, others exhibiting dissolution features at rims or end faces.

Figure 3. Iron sulfide mineralization in dissolution-induced cavities in olivine (SEM). (a) Cavity resembles negative olivine crystal shape, with iron sulfide mineralization as conjoined, planar aggregates. (b) In contrast to olivine (right side), volcanic glass displays only slightly corroded surfaces with small etch pits. (c) Iron sulfide growth (serrate marcasite and euhedral spinel) on volcanic glass surface.

Figure 4. BSE images from a thin section depicts iron sulfide precipitation (white) inside cavities created by olivine dissolution. Key: Pl, plagioclase; Ol, olivine; Spl, spinel. (a) Even in cavities completely devoid of olivine, iron sulfide precipitation is organized in

Always consult and cite the final, published document. See http:/www.minsocam.org or GeoscienceWorld

This is the peer-reviewed, final accepted version for American Mineralogist, published by the Mineralogical Society of America.
The published version is subject to change. Cite as Authors (Year) Title. American Mineralogist, in press.
DOI: https://doi.org/10.2138/am-2022-8057. http://www.minsocam.org/

554 conjoined aggregates, forming a bead chain aspect in profile. (b) Mineralization in the
555 center of a tubular void in an olivine crystal. (c) Iron sulfide precipitation does not occur
556 deliberately, and is minor or lacking on volcanic glass surfaces (neither on dissolving
557 olivine). It does occur on some spinel surfaces, as can be seen in (a).
558
559 **Figure 5.** Occurrence and connectivity of voids inside a volcanic ash particle (3D X-ray
560 microscopy, XRM). ($a_{1,2}$) Visualization of pore space (blue) in the volume reconstruction
561 of an ash particle consisting of a single olivine grain and glass matrix attached. Note that
562 this sample was analyzed with SEM in Fig. 3a. ($b_{1,2,3}$). Reconstructed slices at different
563 levels, displaying the bead chain aspect of iron sulfide mineralization and the location of
564 these structures aligned in the center of the cavities. Note the occurrence of spinel in
565 these aggregates. (c) Location of a high-resolution scan inside this particle (see Fig. 8a,
566 b). Please compare also supplementary figure S1.
567
568 **Figure 6.** Raman spectra at selected locations on the polished thin section. (a) In most of
569 the analyzed locations, the baseline-corrected and normalized spectra reveal the presence
570 of both pyrite and marcasite in varying proportions. In some locations concomitant
571 red/blue-shift of the frequencies has been observed for both phases irrespective of their
572 proportions, which we explain in terms of slightly different average crystallite sizes.
573 Colored letters A, B, E and T with indices indicate Raman vibrational modes for pyrite
574 and marcasite (colored vertical bars); see text for details. (b)-(d) BSE image with
575 locations G1-01 to G1-12 (b), G1-13 to G1-16 (c), and G2-01 to G2-03, respectively.
576 Phase proportions are indicated by pie charts.

Always consult and cite the final, published document. See http:/www.minsocam.org or GeoscienceWorld

This is the peer-reviewed, final accepted version for American Mineralogist, published by the Mineralogical Society of America.
The published version is subject to change. Cite as Authors (Year) Title. American Mineralogist, in press.
DOI: https://doi.org/10.2138/am-2022-8057. http://www.minsocam.org/

577

578 **Figure 7.** 2D and 3D quantitative image analysis of iron sulfide precipitation (yellow)
579 inside cavities (blue) created by olivine dissolution. (a)-(e) 2D analyses of selected
580 cavities using BSE images. ($f_{1,2}$) and ($g_{1,2}$) 3D analyses of selected cavities using
581 reconstructed XRM scans.

582

583 **Figure 8.** Results from high-resolution XRM scans showing microfabric of olivine
584 dissolution and FeS_2 precipitation processes, with particular consideration of spinel
585 occurrence. Key: Spl, spinel; Sf, sulfide. (a) Semitransparent rendering of olivine (green)
586 and iron sulfide reveals presence of spinel inside the FeS_2 precipitates (a_1, a_4). a_2: Opaque
587 rendering of this layer highlights the serrate characteristic of iron sulfide in this particular
588 piece (see also Fig. 3a). a_3: 3D view of a olivine dissolution surface, encompassing the
589 iron sulfide mineralization. Note the tiny bridges that in places connect the sulfide layer
590 with the retreated olivine dissolution surface. (b) Reconstructed image slices of the
591 volume of interest in (a) unveil sulfide growth features, such as nucleation sites both on
592 spinel and filamentous structures, development of cavities around spinel grains near the
593 olivine dissolution surface, the organization of iron sulfide aggregates, and spinel crystals
594 enclosed therein. For localization of the high-resolution scan please refer to Fig. 5. Please
595 compare also supplementary figure S3.

596

597 **Figure 9.** Conceptual model for rapid olivine dissolution and iron sulfide formation**.** (a)
598 Cartoon representation of the chemical environment for rapid olivine dissolution and iron
599 sulfide formation. Widespread occurrence of shells of vesicomyid clams (genus

Always consult and cite the final, published document. See http:/www.minsocam.org or GeoscienceWorld

This is the peer-reviewed, final accepted version for American Mineralogist, published by the Mineralogical Society of America.
The published version is subject to change. Cite as Authors (Year) Title. American Mineralogist, in press.
DOI: https://doi.org/10.2138/am-2022-8057. http://www.minsocam.org/

Abyssogena) at the sampling site indicate the presence of sulfide-rich fluids. (b-e) Iron sulfide formation involves: (b) development of cracks in olivine, preferentially around spinel, (c) infiltration of reducing sulfide-bearing solutions and initiation of olivine dissolution, (d) heterogeneous nucleation of FeS_2 preferably as pyrite on spinel and continued growth of FeS_2 aggregates. (e) Eventually, colonization of sulfate-reducing bacteria may add an additional path for microbial iron fixation.

Figure 10. Results of a reaction path model calculation showing the possible timing of pyrite (or marcasite) formation. See text for model details.

Supplementary figures: S1, S2, S3.

Always consult and cite the final, published document. See http:/www.minsocam.org or GeoscienceWorld

This is the peer-reviewed, final accepted version for American Mineralogist, published by the Mineralogical Society of America.
The published version is subject to change. Cite as Authors (Year) Title. American Mineralogist, in press.
DOI: https://doi.org/10.2138/am-2022-8057. http://www.minsocam.org/

611 **Table Captions**

612

613 **Table 1.** Average olivine, spinel and sulfide analyses of the investigated samples. See
614 also Table S1-3 in supplementary online material for individual analyses.

Olivine (N=33) wt%	SiO2	Al2O3	FeO	MnO	MgO	CaO	NiO	Total	Fo%
Average	39.33	0.05	17.68	0.26	43.64	0.32	0.23	101.6	81.5
Std.dev.	0.20	0.01	0.68	0.03	0.53	0.05	0.03	0.24	0.76

Sulfide (N=27) wt%	Mn	Fe	Ni	As	Cu	Co	Zn	Pb	Sb	S	Total
Average	0.939	43.66	0.535	0.049	0.007	0.016	0.042	0.178	0.010	52.64	98.07
Std.dev.	0.450	0.46	0.118	0.021	0.013	0.014	0.019	0.069	0.015	0.65	0.80

Spinel (N=19) wt%	MgO	CaO	TiO2	Cr2O3	FeO,tot	MnO	SiO2	Al2O3	Total	Cr#	Mg#
Average	10.07	0.041	4.383	24.421	38.567	0.297	0.080	17.684	95.547	48.30	45.04
Std.dev.	0.811	0.037	1.120	1.714	3.299	0.039	0.034	2.595	0.737	2.45	3.85

afu per 3 cats.	Mg	Ti	Cr	Fe3+	Fe2+	Mn	Al	cations	oxygens
Average	0.495	0.109	0.636	0.460	0.606	0.008	0.686	3.000	4.000
Std.dev.	0.030	0.030	0.034	0.056	0.059	0.001	0.088		

615

616

Always consult and cite the final, published document. See http:/www.minsocam.org or GeoscienceWorld

This is the peer-reviewed, final accepted version for American Mineralogist, published by the Mineralogical Society of America.
The published version is subject to change. Cite as Authors (Year) Title. American Mineralogist, in press.
DOI: https://doi.org/10.2138/am-2022-8057. http://www.minsocam.org/

Table 2: Raman fit frequencies (±0.1 cm^{-1}) and their assignments for the respective symmetry species obtained from the deconvoluted spectra of FeS_2 at selected locations of the polished thin sections as labeled in Fig. 6. The symmetry species of the pyrite (Py) and marcasite (Mrc) are given.

Location (grain, spot)	A_g(Mrc) /B_{2g}(Mrc) /B_{3g}(Mrc)	E_g(Py)	T_g(Py)	A_g(Py) /T_g(Py)	A_g(Mrc)	B_{1g}(Mrc)	T_g(Py)	B_{1g}(Mrc)	Py /%	Mrc / %
G1-01	319.51	336.92	355.19	373.36	379.81	-	418.75	-	63	37
G1-02	324.05	339.05	352.68	378.81	-	393.82	423.80	463.12	53	47
G1-03	320.98	339.82	344.98	382.92	381.15	-	426.52	-	43	57
G1-04	321.15	338.95	352.23	378.48	-	398.00	423.64	-	44	56
G1-05	324.03	339.74	361.46	376.24	385.58	398.27	420.91	-	41	59
G1-06	318.41	337.64	354.92	373.28	379.69	396.61	419.77	452.43	24	76
G1-07	317.54	336.28	354.07	372.18	380.42	-	415.68	446.30	52	48
G1-08	319.26	336.80	353.09	373.73	378.56	398.00	417.68	-	47	53
G1-09	319.17	338.57	354.15	378.15	390.75	398.00	421.89	-	18	82
G1-10	323.22	339.35	352.02	378.88	-	390.35	425.46	-	39	61
G1-11	-	342.21	350.20	378.61	389.56	-	429.31	-	100	0
G1-12	324.56	341.71	360.00	380.05	386.85	-	426.23	-	40	60
G1-13	324.00	342.19	350.00	380.00	388.00	401.24	430.22	-	89	11
G1-14	-	348.76	-	385.32	-	395.22	438.85	-	100	0
G1-15	326.10	343.96	361.46	380.52	385.98	399.92	427.56	-	47	53
G1-16	324.86	343.10	361.76	380.43	387.54	401.75	426.00	-	24	76
G2-01	324.56	341.71	360.00	378.00	380.05	386.85	426.23	-	3	97
G2-02	322.39	339.97	357.12	376.26	385.94	398.00	423.87	-	30	70
G2-03	324.19	342.16	356.95	379.62	383.65	398.00	427.81	-	39	61

Always consult and cite the final, published document. See http:/www.minsocam.org or GeoscienceWorld

This is the peer-reviewed, final accepted version for American Mineralogist, published by the Mineralogical Society of America.
The published version is subject to change. Cite as Authors (Year) Title. American Mineralogist, in press.
DOI: https://doi.org/10.2138/am-2022-8057. http://www.minsocam.org/

622 **Table 3.** Percentage of iron sulfide content in relation to the hosting cavity.

Cavity description	Sulfide area% /vol%	Source	Part of Fig. 7
Ol in thin section	24.0	BSE	a
Ol in thin section	17.4	BSE	b
Ol in thin section	19.9	BSE	c
Ol in thin section	20.8	BSE	d
Ol in thin section	18.0	BSE	e
Largest void in single Ol grain	18.1	XRM	f_1
2nd largest void in single Ol grain	19.4	XRM	f_2
Largest connected void, spanning over multiple olivines	4.2	XRM	g_1
Close-up of the above	10.1	XRM	g_2

623 Abbreviations: Ol - olivine, BSE - back-scattered image (2D quantitative image analysis),
624 XRM - 3D X-ray microscopy (3D quantitative image analysis).

625

626

627 **Tables (Supplementary files):**

628 Table S1: Olivine analyses.

629 Table S2: Spinel analyses.

630 Table S3: Sulfide analyses.

631

632

Always consult and cite the final, published document. See http:/www.minsocam.org or GeoscienceWorld

This is the peer-reviewed, final accepted version for American Mineralogist, published by the Mineralogical Society of America.
The published version is subject to change. Cite as Authors (Year) Title. American Mineralogist, in press.
DOI: https://doi.org/10.2138/am-2022-8057. http://www.minsocam.org/

633 **REFERENCES CITED**

634

635 Alt, J.C. (1988) Hydrothermal oxide and nontronite deposits on seamounts in the
636 eastern Pacific. Marine Geology, 81(1), 227-239.
637 -. (1995) Subseafloor Processes in Mid-Ocean Ridge Hydrothennal Systems. Seafloor
638 Hydrothermal Systems: Physical, Chemical, Biological, and Geological
639 Interactions, p. 85-114.
640 Barbee, O., Chesner, C., and Deering, C. (2020) Quartz crystals in Toba rhyolites
641 show textures symptomatic of rapid crystallization. American Mineralogist,
642 105(2), 194-226.
643 Bazylinski, D.A., and Frankel, R.B. (2003) Biologically controlled mineralization in
644 prokaryotes. Biomineralization, 54, 217-247.
645 Bethke, C.M. (1996) Geochemical Reaction Modeling. Oxford University Press, New
646 York.
647 Bryant, R.N., Pasteris, J.D., and Fike, D.A. (2017) Variability in the Raman Spectrum
648 of Unpolished Growth and Fracture Surfaces of Pyrite Due to Laser Heating
649 and Crystal Orientation. Applied Spectroscopy, 72(1), 37-47.
650 Chan, C.S., Fakra, S.C., Emerson, D., Fleming, E.J., and Edwards, K.J. (2011)
651 Lithotrophic iron-oxidizing bacteria produce organic stalks to control
652 mineral growth: implications for biosignature formation. The ISME Journal,
653 5(4), 717-727.
654 Emerson, D., Rentz, J.A., Lilburn, T.G., Davis, R.E., Aldrich, H., Chan, C., and Moyer, C.L.
655 (2007) A Novel Lineage of Proteobacteria Involved in Formation of Marine
656 Fe-Oxidizing Microbial Mat Communities. Plos One, 2(8).
657 Flaathen, T.K., Gislason, S.R., and Oelkers, E.H. (2010) The effect of aqueous sulphate
658 on basaltic glass dissolution rates. Chemical Geology, 277(3), 345-354.
659 Gee, M.J.R., Watts, A.B., Masson, D.G., and Mitchell, N.C. (2001) Landslides and the
660 evolution of El Hierro in the Canary Islands. Marine Geology, 177(3), 271-
661 293.
662 Gerrits, R., Pokharel, R., Breitenbach, R., Radnik, J., Feldmann, I., Schuessler, J.A., von
663 Blanckenburg, F., Gorbushina, A.A., and Schott, J. (2020) How the rock-
664 inhabiting fungus K. petricola A95 enhances olivine dissolution through
665 attachment. Geochimica et Cosmochimica Acta, 282, 76-97.
666 Gislason, S.R., and Oelkers, E.H. (2003) Mechanism, rates, and consequences of
667 basaltic glass dissolution: II. An experimental study of the dissolution rates of
668 basaltic glass as a function of pH and temperature. Geochimica et
669 Cosmochimica Acta, 67(20), 3817-3832.
670 Gorlas, A., Jacquemot, P., Guigner, J.-M., Gill, S., Forterre, P., and Guyot, F. (2018)
671 Greigite nanocrystals produced by hyperthermophilic archaea of
672 Thermococcales order. PLOS ONE, 13(8), e0201549.
673 Hallbeck, L., and Pedersen, K. (1991) Autotrophic and mixotrophic growth of
674 Gallionella ferruginea. Microbiology, 137(11), 2657-2661.

Always consult and cite the final, published document. See http:/www.minsocam.org or GeoscienceWorld

This is the peer-reviewed, final accepted version for American Mineralogist, published by the Mineralogical Society of America.
The published version is subject to change. Cite as Authors (Year) Title. American Mineralogist, in press.
DOI: https://doi.org/10.2138/am-2022-8057. http://www.minsocam.org/

675 Helgeson, H.C., Delany, J.M., Nesbitt, H.W., and Bird, D.K. (1978) SUMMARY AND
676 CRITIQUE OF THE THERMODYNAMIC PROPERTIES OF ROCK-FORMING
677 MINERALS.
678 Heywood, B.R., Mann, S., and Frankel, R.B. (1991) Structure, Morphology and
679 Growth of Biogenic Greigite (Fe 3 S 4). Materials Research Society
680 Proceedings, 218, 93-108.
681 Hofmann, B.A., Farmer, J.D., von Blanckenburg, F., and Fallick, A.E. (2008) Subsurface
682 filamentous fabrics: an evaluation of origins based on morphological and
683 geochemical criteria, with implications for exopaleontology. Astrobiology,
684 8(1), 87-117.
685 Hunger, S., and Benning, L.G. (2007) Greigite: a true intermediate on the polysulfide
686 pathway to pyrite. Geochemical Transactions, 8(1), 1.
687 Jarosewich, E., Nelen, J., and Norberg, J. (1980) Reference Samples for Electron
688 Microprobe Analysis*. Geostandards Newsletter, 4, 43-47.
689 Jiang, W.-T., Horng, C.-S., Roberts, A.P., and Peacor, D.R. (2001) Contradictory
690 magnetic polarities in sediments and variable timing of neoformation of
691 authigenic greigite. Earth and Planetary Science Letters, 193(1), 1-12.
692 Johnson, J.W., Oelkers, E.H., and Helgeson, H.C. (1992) SUPCRT92: A software
693 package for calculating the standard molal thermodynamic properties of
694 minerals, gases, aqueous species, and reactions from 1 to 5000 bar and 0 to
695 1000°C. Computers & Geosciences, 18(7), 899-947.
696 Klügel, A., Hansteen, T.H., van den Bogaard, P., Strauss, H., and Hauff, F. (2011)
697 Holocene fluid venting at an extinct Cretaceous seamount, Canary
698 archipelago. Geology, 39(9), 855-858.
699 Klügel, A., and Shipboard Scientific, P. (2018) METEOR Fahrtbericht / Cruise Report
700 M146, Henry Seamount Seepage Exploration (HESSE), Recife (Brazil) - Las
701 Palmas de Gran Canaria (Spain), March 17 - April 16, 2018. Gutachterpanel
702 Forschungsschiffe.
703 Klügel, A., Villinger, H., Römer, M., Kaul, N., Krastel, S., Lenz, K.-F., and Wintersteller,
704 P. (2020) Hydrothermal Activity at a Cretaceous Seamount, Canary
705 Archipelago, Caused by Rejuvenated Volcanism. Frontiers in Marine Science,
706 7(1001).
707 Krylova, E.M., Sahling, H., and Janssen, R. (2010) Abyssogena: a new genus of the
708 family Vesicomyidae (bivalvia) Journal of Molluscan Studies, 76, 107-132.
709 Little, C.T.S., Glynn, S.E.J., and Mills, R.A. (2004) Four-Hundred-and-Ninety-Million-
710 Year Record of Bacteriogenic Iron Oxide Precipitation at Sea-Floor
711 Hydrothermal Vents. Geomicrobiology Journal, 21(6), 415-429.
712 Middelburg, J.J. (1989) A simple rate model for organic matter decomposition in
713 marine sediments. Geochimica et Cosmochimica Acta, 53(7), 1577-1581.
714 Murowchick, J.B., and Barnes, H.L. (1986) Marcasite precipitation from
715 hydrothermal solutions. Geochimica et Cosmochimica Acta, 50(12), 2615-
716 2629.
717 Oelkers, E.H., Declercq, J., Saldi, G.D., Gislason, S.R., and Schott, J. (2018) Olivine
718 dissolution rates: A critical review. Chemical Geology, 500, 1-19.
719 Oelkers, E.H., and Gislason, S.R. (2001) The mechanism, rates and consequences of
720 basaltic glass dissolution: I. An experimental study of the dissolution rates of

Always consult and cite the final, published document. See http:/www.minsocam.org or GeoscienceWorld

This is the peer-reviewed, final accepted version for American Mineralogist, published by the Mineralogical Society of America.
The published version is subject to change. Cite as Authors (Year) Title. American Mineralogist, in press.
DOI: https://doi.org/10.2138/am-2022-8057. http://www.minsocam.org/

basaltic glass as a function of aqueous Al, Si and oxalic acid concentration at 25°C and pH = 3 and 11. Geochimica et Cosmochimica Acta, 65(21), 3671-3681.

Passier, H.F., Middelburg, J.J., de Lange, G.J., and Böttcher, M.E. (1997) Pyrite contents, microtextures, and sulfur isotopes in relation to formation of the youngest eastern Mediterranean sapropel. Geology, 25(6), 519-522.

Posfai, M., Buseck, P.R., Bazylinski, D.A., and Frankel, R.B. (1998) Iron sulfides from magnetotactic bacteria; structure, composition, and phase transitions. American Mineralogist, 83(11-12_Part_2), 1469-1481.

Qian, G., Xia, F., Brugger, J., Skinner, W.M., Bei, J., Chen, G., and Pring, A. (2011) Replacement of pyrrhotite by pyrite and marcasite under hydrothermal conditions up to 220 °C: An experimental study of reaction textures and mechanisms. American Mineralogist, 96(11-12), 1878-1893.

Rickard, D. (2012) Chapter 5 - Metastable Sedimentary Iron Sulfides. In D. Rickard, Ed. Developments in Sedimentology, 65, p. 195-231. Elsevier.

Rimstidt, J.D., Brantley, S.L., and Olsen, A.A. (2012) Systematic review of forsterite dissolution rate data. Geochimica et Cosmochimica Acta, 99, 159-178.

Roberts, A.P. (2015) Magnetic mineral diagenesis. Earth-Science Reviews, 151, 1-47.

Roberts, A.P., Jiang, W.-T., Florindo, F., Horng, C.-S., and Laj, C. (2005) Assessing the timing of greigite formation and the reliability of the Upper Olduvai polarity transition record from the Crostolo River, Italy. Geophysical Research Letters, 32(5).

Schoonen, M.A.A., and Barnes, H.L. (1991) Reactions forming pyrite and marcasite from solution: I. Nucleation of FeS2 below 100°C. Geochimica et Cosmochimica Acta, 55(6), 1495-1504.

Slack, J.F., Grenne, T., Bekker, A., Rouxel, O.J., and Lindberg, P.A. (2007) Suboxic deep seawater in the late Paleoproterozoic: Evidence from hematitic chert and iron formation related to seafloor-hydrothermal sulfide deposits, central Arizona, USA. Earth and Planetary Science Letters, 255(1), 243-256.

Stefánsson, A., Arnórsson, S., Gunnarsson, I., Kaasalainen, H., and Gunnlaugsson, E. (2011) The geochemistry and sequestration of H2S into the geothermal system at Hellisheidi, Iceland. Journal of Volcanology and Geothermal Research, 202(3), 179-188.

Thiel, J., Byrne, J.M., Kappler, A., Schink, B., and Pester, M. (2019) Pyrite formation from FeS and H2S is mediated through microbial redox activity. Proceedings of the National Academy of Sciences, 116(14), 6897.

Titschack, J., Baum, D., Matsuyama, K., Boos, K., Färber, C., Kahl, W.A., Ehrig, K., Meinel, D., Soriano, C., and Stock, S.R. (2018) Ambient occlusion – A powerful algorithm to segment shell and skeletal intrapores in computed tomography data. Computers & Geosciences, 115, 75-87.

Toplis, M.J. (2005) The thermodynamics of iron and magnesium partitioning between olivine and liquid: criteria for assessing and predicting equilibrium in natural and experimental systems. Contributions to Mineralogy and Petrology, 149(1), 22-39.

Always consult and cite the final, published document. See http:/www.minsocam.org or GeoscienceWorld

This is the peer-reviewed, final accepted version for American Mineralogist, published by the Mineralogical Society of America.
The published version is subject to change. Cite as Authors (Year) Title. American Mineralogist, in press.
DOI: https://doi.org/10.2138/am-2022-8057. http://www.minsocam.org/

765 Vigliaturo, R., Marengo, A., Bittarello, E., Pérez-Rodríguez, I., Dražić, G., and Gieré, R.
766 (2020) Micro- and nano-scale mineralogical characterization of Fe(II)-
767 oxidizing bacterial stalks. Geobiology.
768 Vogt, H., Chattopadhyay, T., and Stolz, H.J. (1983) Complete first-order Raman
769 spectra of the pyrite structure compounds FeS2, MnS2 AND SiP2. Journal of
770 Physics and Chemistry of Solids, 44(9), 869-873.
771 Welch, S.A., and Banfield, J.F. (2002) Modification of olivine surface morphology and
772 reactivity by microbial activity during chemical weathering. Geochimica et
773 Cosmochimica Acta, 66(2), 213-221.
774 Welsch, B., Faure, F., Famin, V., Baronnet, A., and Bachèlery, P. (2012) Dendritic
775 Crystallization: A Single Process for all the Textures of Olivine in Basalts?
776 Journal of Petrology, 54(3), 539-574.
777 Wiggering, H., Neumann-Mahlkau, P., and Selbach, H.-J. (1992) Experimental
778 Procedures to Simulate Weathering Under Atmospheres Which May Have
779 Characterized the Early Archean. In M. Schidlowski, S. Golubic, M.M.
780 Kimberley, D.M. McKirdy, and P.A. Trudinger, Eds. Early Organic Evolution:
781 Implications for Mineral and Energy Resources, p. 31-40. Springer Berlin
782 Heidelberg, Berlin, Heidelberg.
783 Wolery, T.J., and Jove-Colon, C.F. (2004) Qualification of Thermodynamic Data for
784 Geochemical Modeling of Mineral-Water Interactions in Dilute Systems,
785 United States.
786 Xi, S., Zhang, X., Luan, Z., Du, Z., Li, L., Liang, Z., Lian, C., and Yan, J. (2019) Micro-
787 Raman Study of Thermal Transformations of Sulfide and Oxysalt Minerals
788 Based on the Heat Induced by Laser. Minerals, 9(12).
789 Yao, X., Xia, F., Brugger, J., Kartal, M., and Adegoke, I.A. (2021) Rapid Marcasite to
790 Pyrite Transformation in Acidic Low-Temperature Hydrothermal Fluids and
791 Saturation Index Control on FeS2 Precipitation Dynamics and Phase
792 Selection. ACS Earth and Space Chemistry.
793 Yao, X., Xia, F., Deditius, A.P., Brugger, J., Etschmann, B.E., Pearce, M.A., and Pring, A.
794 (2020) The mechanism and kinetics of the transformation from marcasite to
795 pyrite: in situ and ex situ experiments and geological implications.
796 Contributions to Mineralogy and Petrology, 175(3), 27.
797

Always consult and cite the final, published document. See http:/www.minsocam.org or GeoscienceWorld

This is the peer-reviewed, final accepted version for American Mineralogist, published by the Mineralogical Society of America.
The published version is subject to change. Cite as Authors (Year) Title. American Mineralogist, in press.
DOI: https://doi.org/10.2138/am-2022-8057. http://www.minsocam.org/

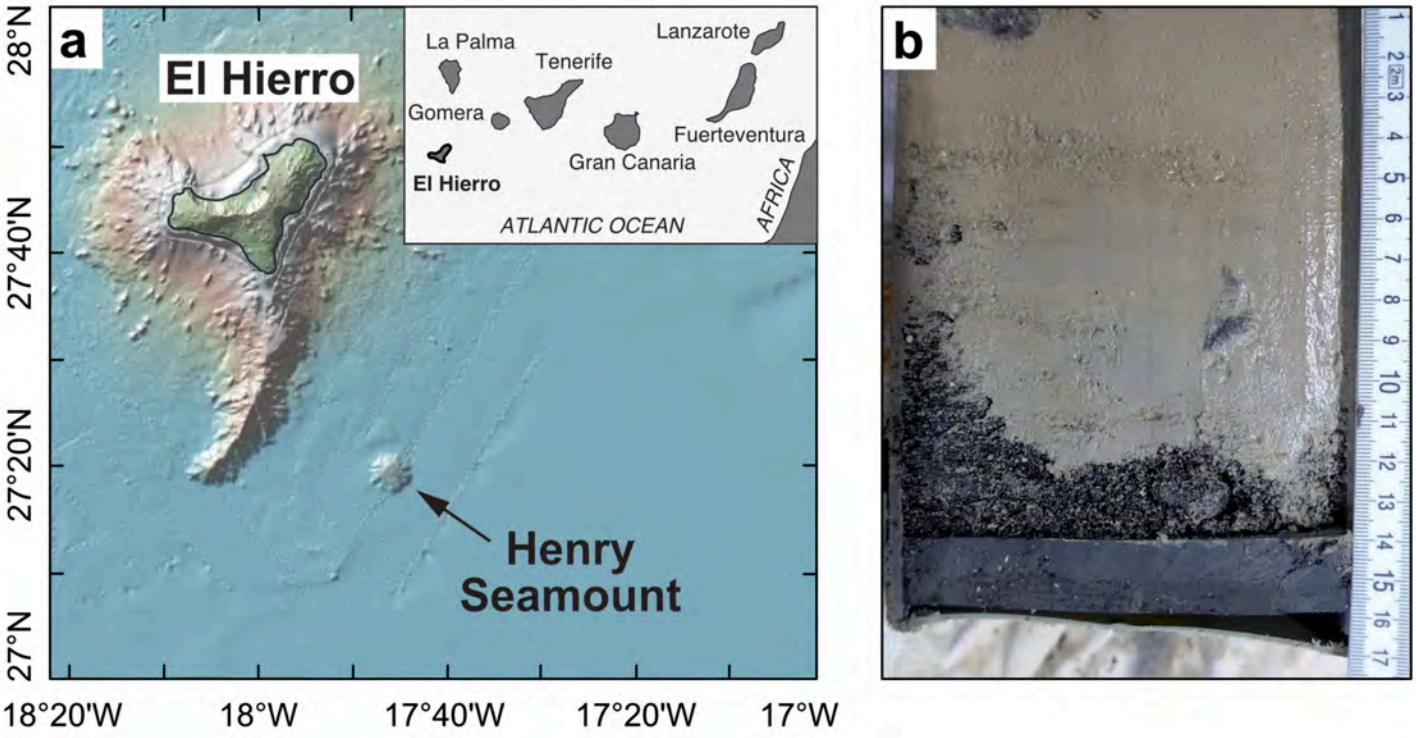

Figure 1

Always consult and cite the final, published document. See http:/www.minsocam.org or GeoscienceWorld

This is the peer-reviewed, final accepted version for American Mineralogist, published by the Mineralogical Society of America.
The published version is subject to change. Cite as Authors (Year) Title. American Mineralogist, in press.
DOI: https://doi.org/10.2138/am-2022-8057. http://www.minsocam.org/

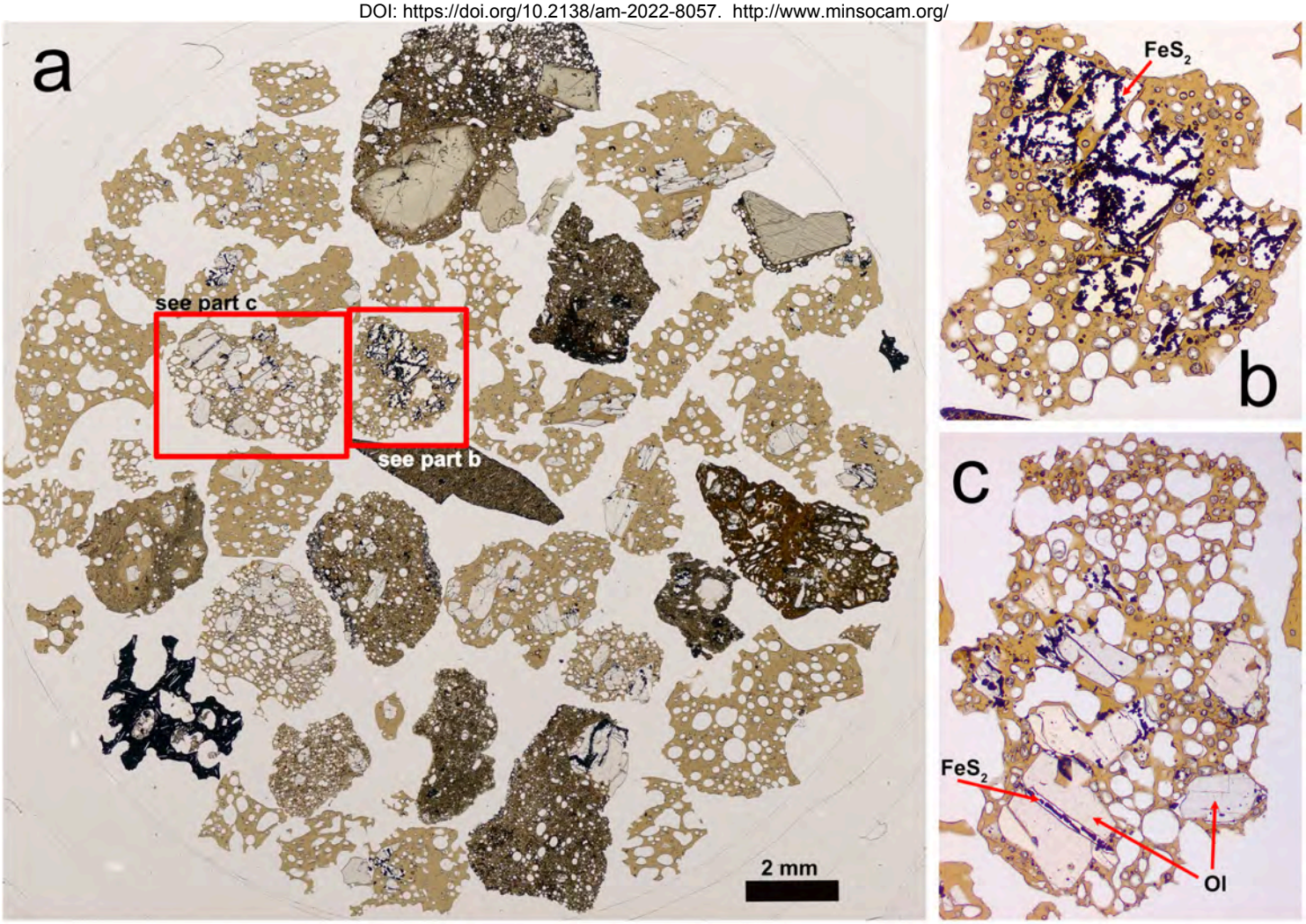

Figure 2

Always consult and cite the final, published document. See http:/www.minsocam.org or GeoscienceWorld

This is the peer-reviewed, final accepted version for American Mineralogist, published by the Mineralogical Society of America.
The published version is subject to change. Cite as Authors (Year) Title. American Mineralogist, in press.
DOI: https://doi.org/10.2138/am-2022-8057. http://www.minsocam.org/

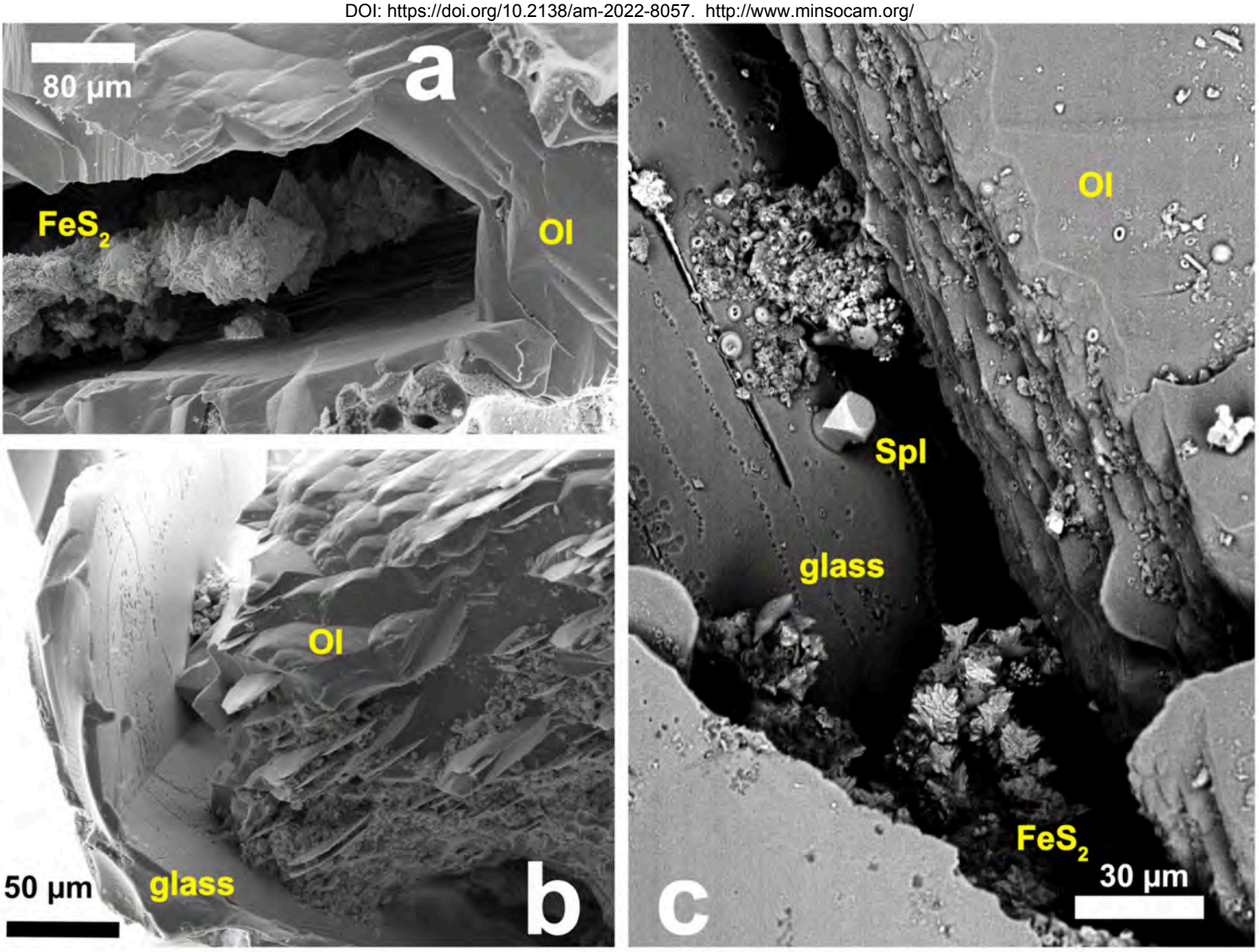

Figure 3

Always consult and cite the final, published document. See http:/www.minsocam.org or GeoscienceWorld

This is the peer-reviewed, final accepted version for American Mineralogist, published by the Mineralogical Society of America.
The published version is subject to change. Cite as Authors (Year) Title. American Mineralogist, in press.
DOI: https://doi.org/10.2138/am-2022-8057. http://www.minsocam.org/

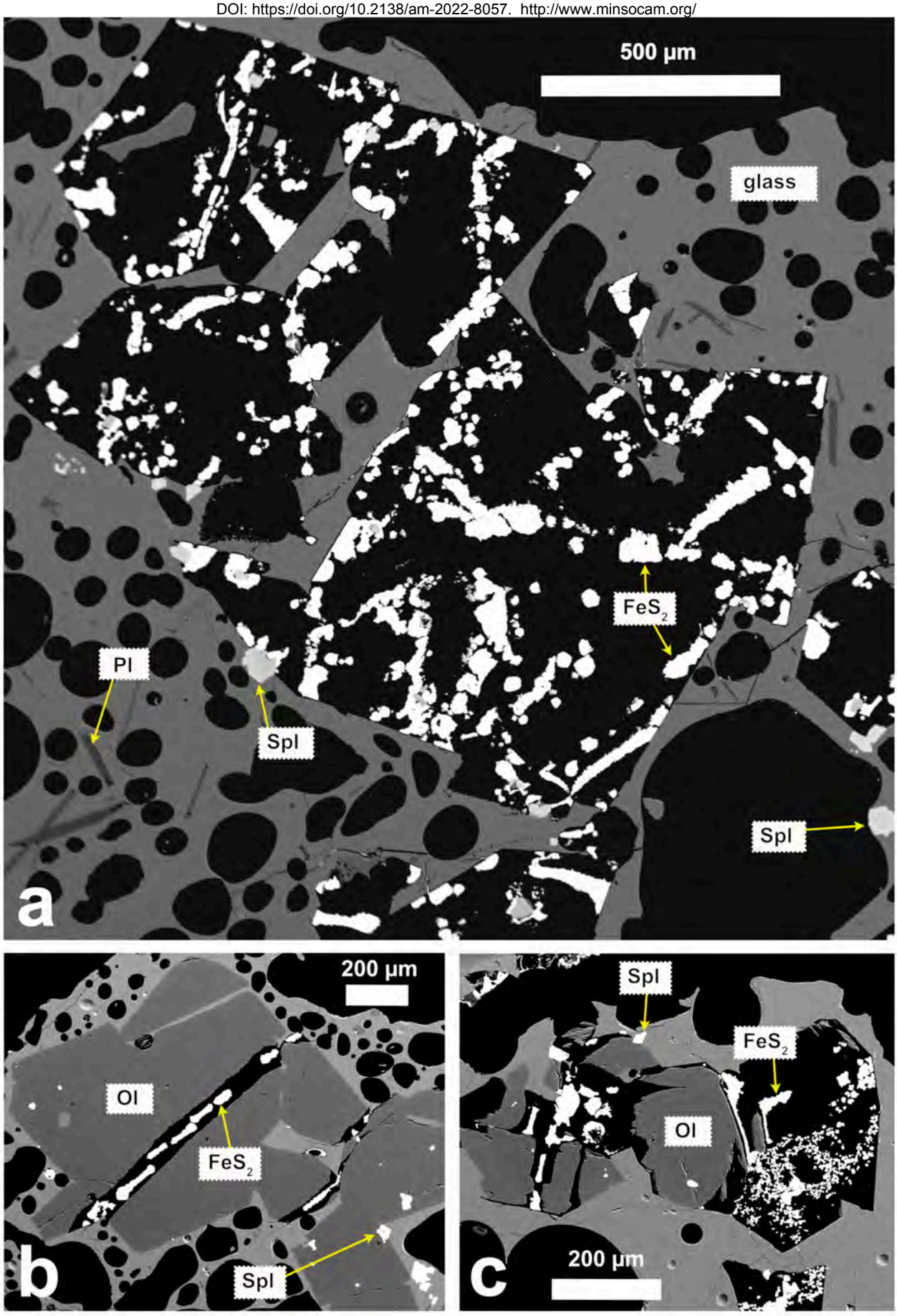

Figure 4

Always consult and cite the final, published document. See http:/www.minsocam.org or GeoscienceWorld

This is the peer-reviewed, final accepted version for American Mineralogist, published by the Mineralogical Society of America.
The published version is subject to change. Cite as Authors (Year) Title. American Mineralogist, in press.
DOI: https://doi.org/10.2138/am-2022-8057. http://www.minsocam.org/

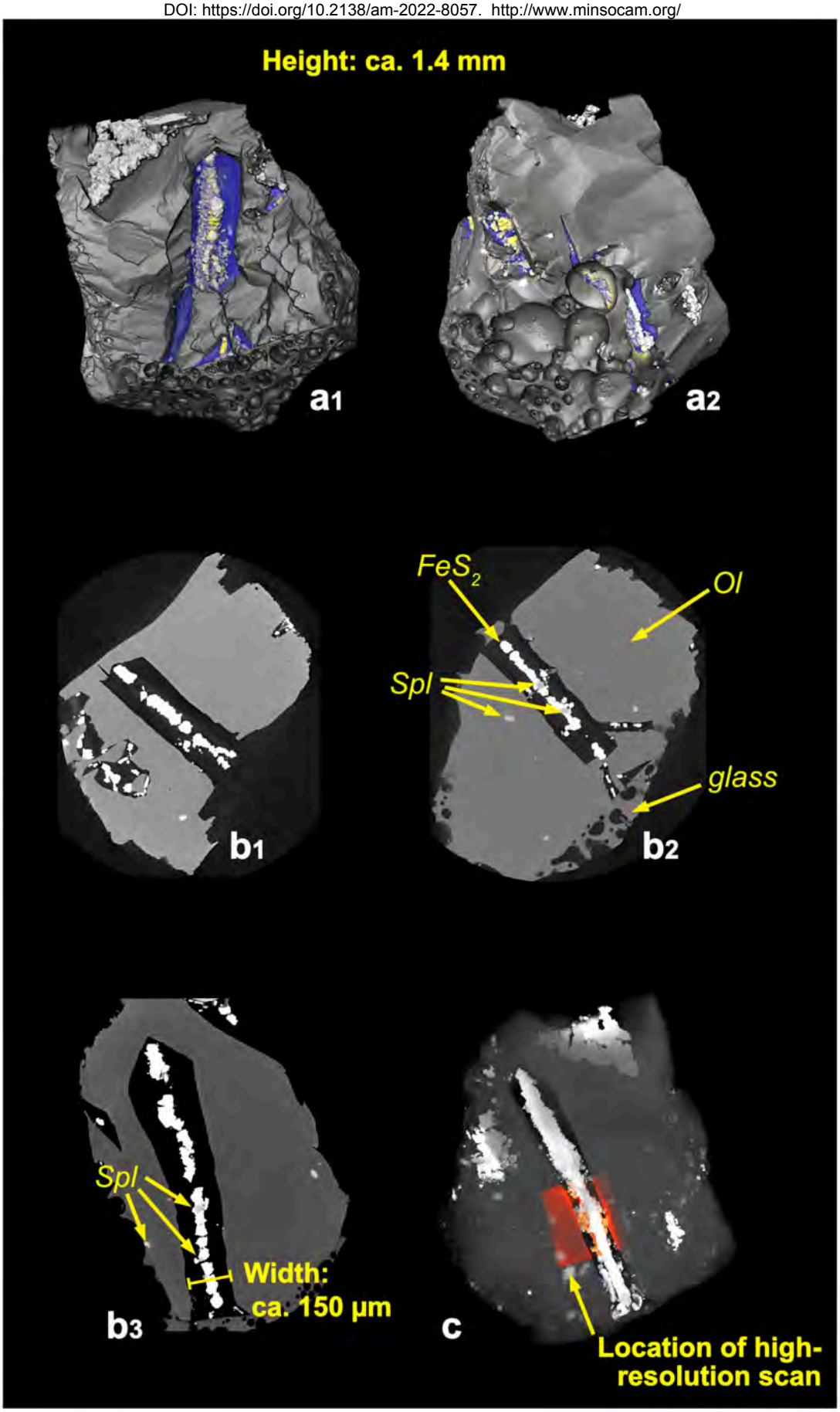

Figure 5

Always consult and cite the final, published document. See http:/www.minsocam.org or GeoscienceWorld

This is the peer-reviewed, final accepted version for American Mineralogist, published by the Mineralogical Society of America.
The published version is subject to change. Cite as Authors (Year) Title. American Mineralogist, in press.
DOI: https://doi.org/10.2138/am-2022-8057. http://www.minsocam.org/

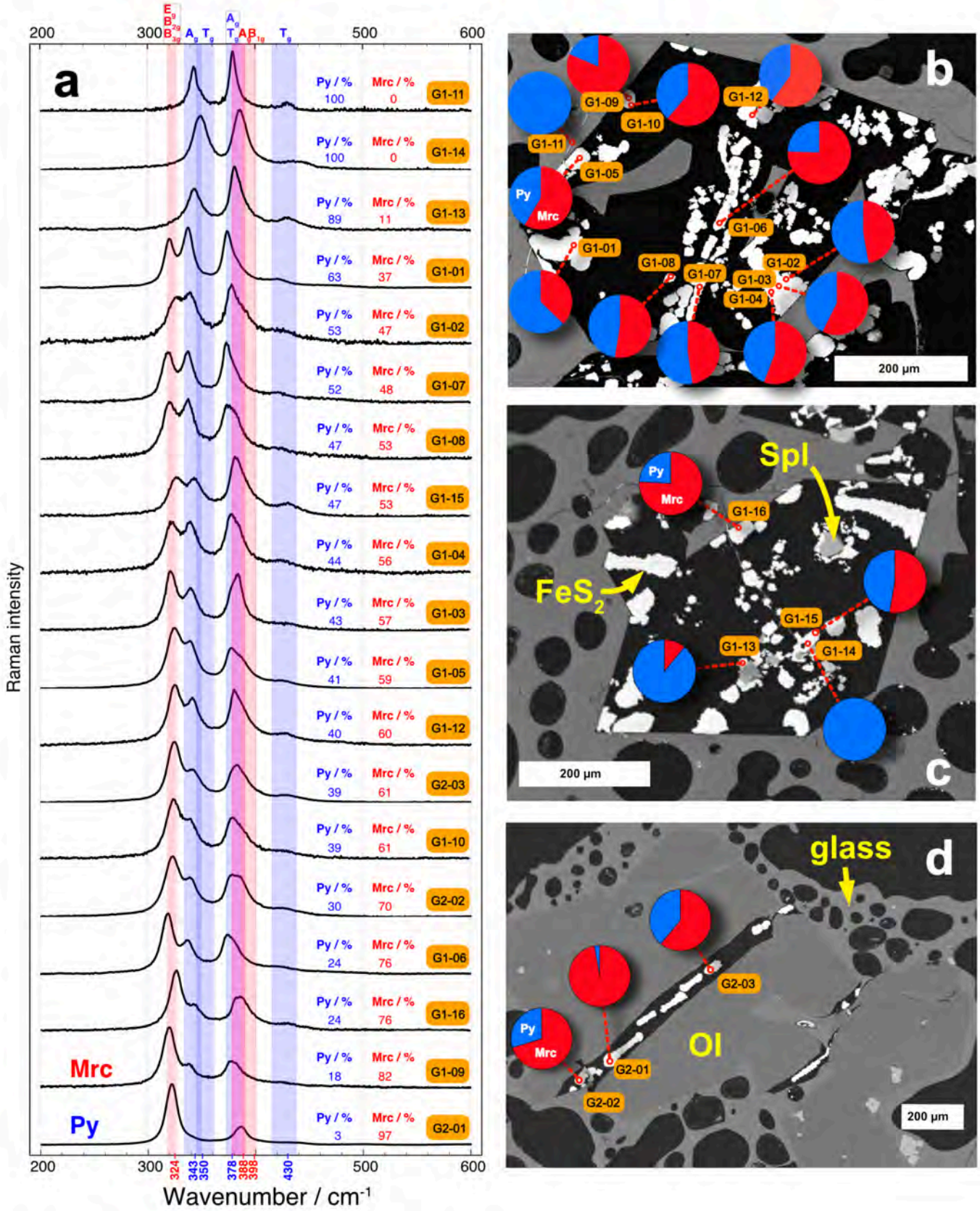

Figure 6

Always consult and cite the final, published document. See http:/www.minsocam.org or GeoscienceWorld

This is the peer-reviewed, final accepted version for American Mineralogist, published by the Mineralogical Society of America.
The published version is subject to change. Cite as Authors (Year) Title. American Mineralogist, in press.
DOI: https://doi.org/10.2138/am-2022-8057. http://www.minsocam.org/

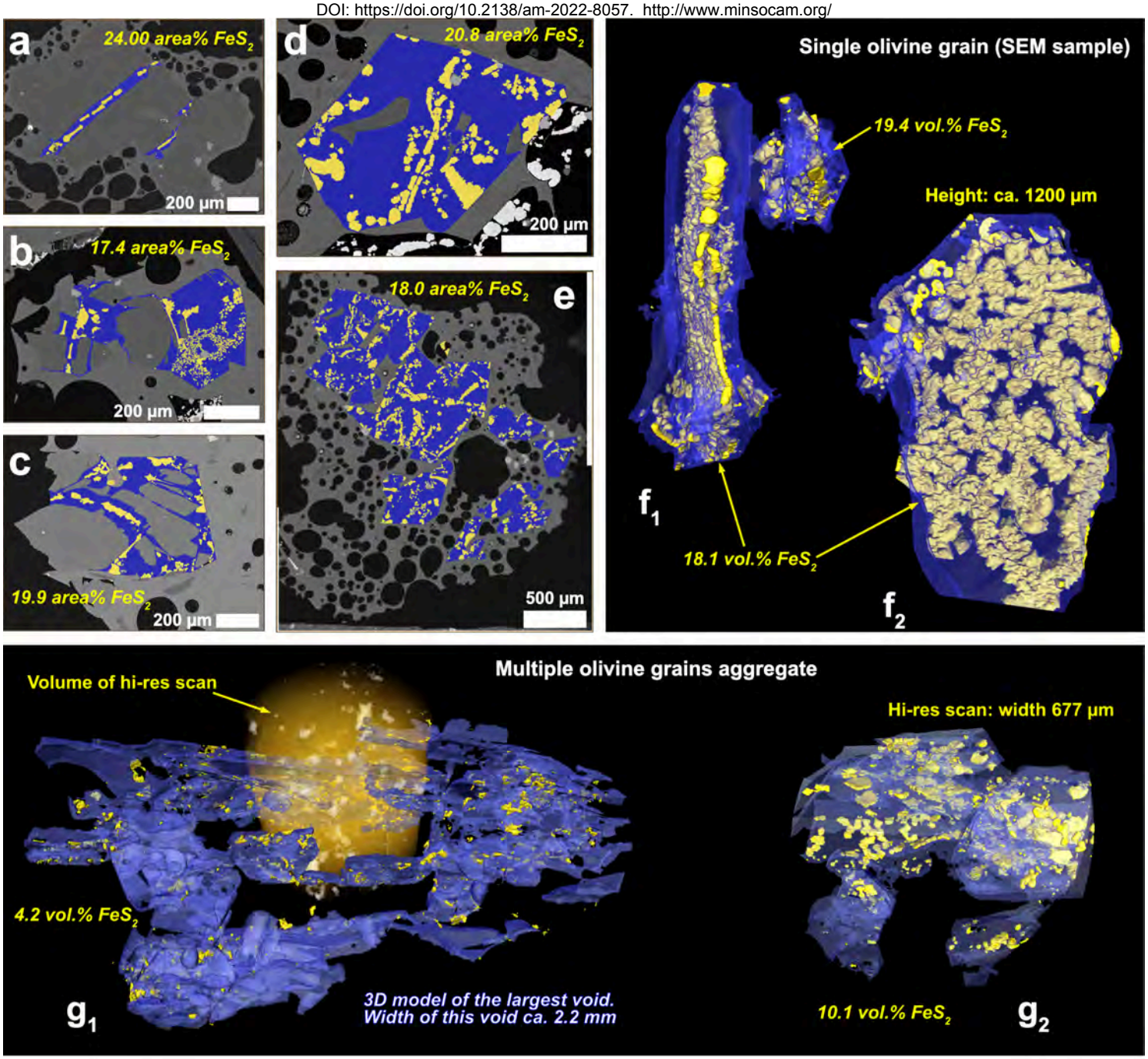

Figure 7

Always consult and cite the final, published document. See http:/www.minsocam.org or GeoscienceWorld

This is the peer-reviewed, final accepted version for American Mineralogist, published by the Mineralogical Society of America.
The published version is subject to change. Cite as Authors (Year) Title. American Mineralogist, in press.
DOI: https://doi.org/10.2138/am-2022-8057. http://www.minsocam.org/

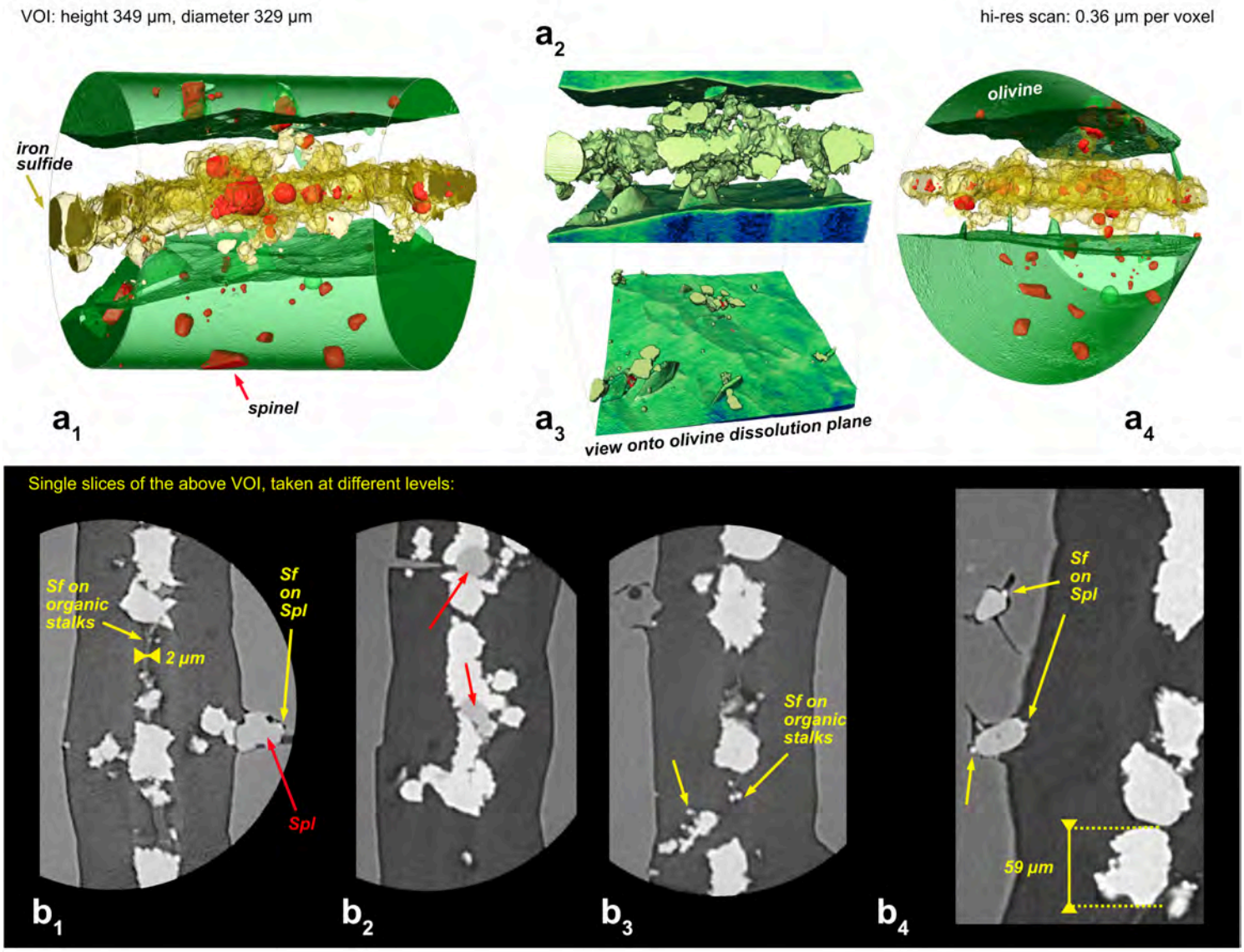

Figure 8

Always consult and cite the final, published document. See http:/www.minsocam.org or GeoscienceWorld

This is the peer-reviewed, final accepted version for American Mineralogist, published by the Mineralogical Society of America.
The published version is subject to change. Cite as Authors (Year) Title. American Mineralogist, in press.
DOI: https://doi.org/10.2138/am-2022-8057. http://www.minsocam.org/

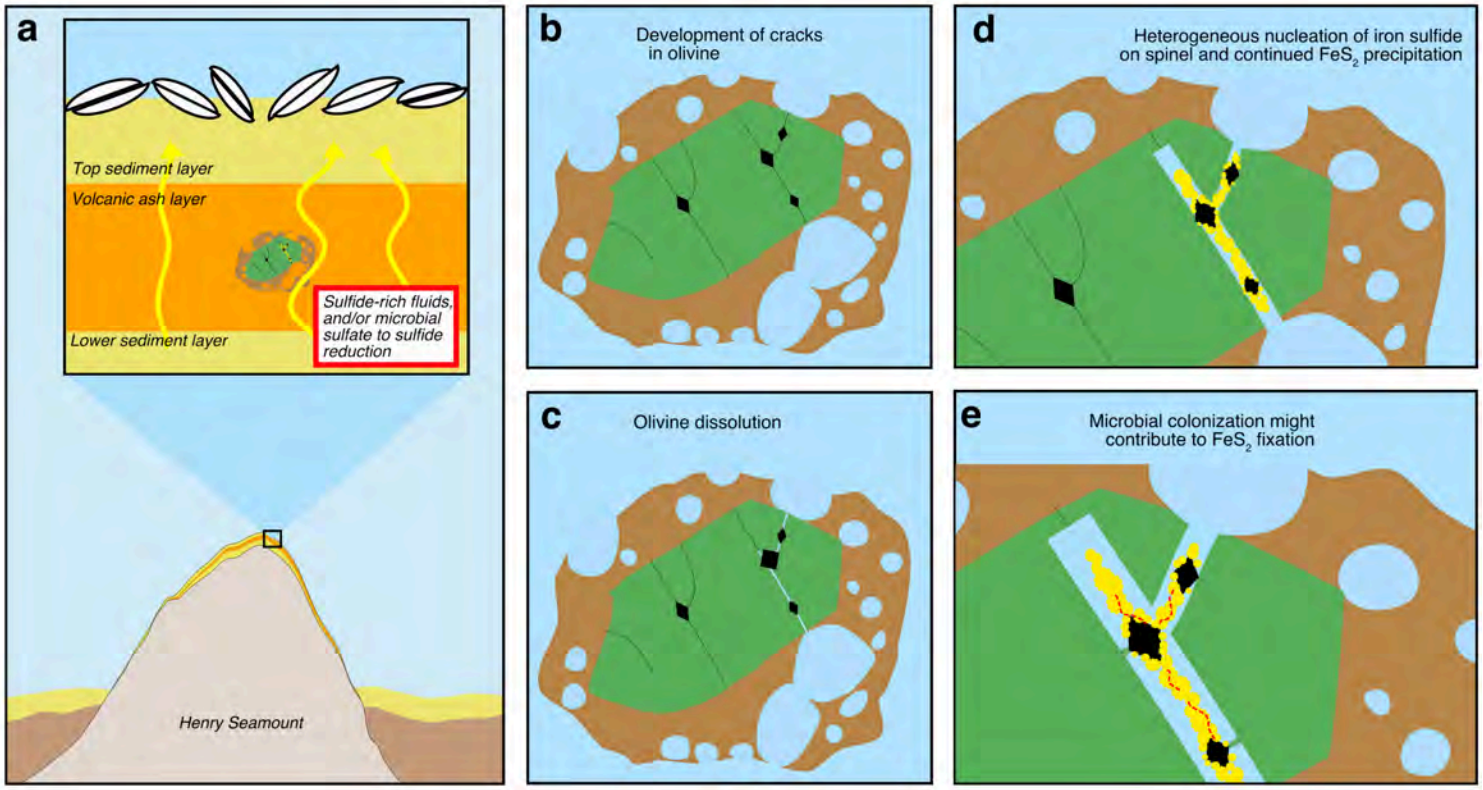

Figure 9

Always consult and cite the final, published document. See http:/www.minsocam.org or GeoscienceWorld

This is the peer-reviewed, final accepted version for American Mineralogist, published by the Mineralogical Society of America.
The published version is subject to change. Cite as Authors (Year) Title. American Mineralogist, in press.
DOI: https://doi.org/10.2138/am-2022-8057. http://www.minsocam.org/

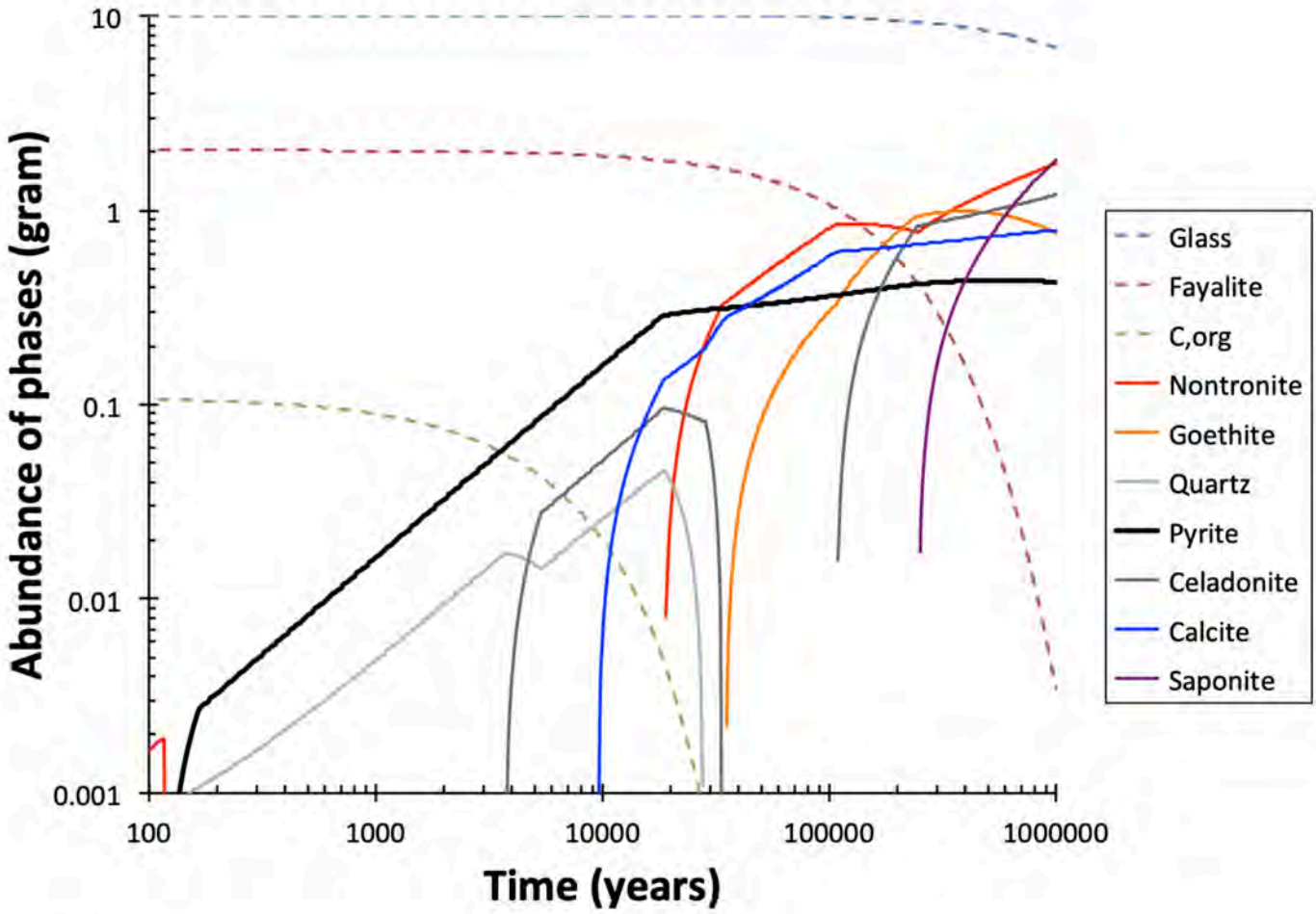

Figure 10

Always consult and cite the final, published document. See http:/www.minsocam.org or GeoscienceWorld